INSTITUT NATIONAL DE RECHERCHE EN INFORMATIQUE ET EN AUTOMATIQUE

Automated Analysis of Basal Ganglia Intensity Distribution in Multisequence MRI of the Brain - Application to Creutzfeldt-Jakob Disease

Marius George Linguraru — Miguel Ángel González Ballester — Eric Bardinet — Damien Galanaud — Stephane Haïk — Baptiste Faucheux — Jean Jaques Hauw — Patrick Cozzone — Didier Dormont — Jean-Philippe Brandel — Nicholas Ayache

N° ????

July 2004

Thème ?

ISSN 0249-6399

Automated Analysis of Basal Ganglia Intensity Distribution in Multisequence MRI of the Brain - Application to Creutzfeldt-Jakob Disease

Marius George Linguraru* , Miguel Ángel González Ballester *, Eric Bardinet † , Damien Galanaud ‡ § , Stephane Haïk ¶ ‖ , Baptiste Faucheux ¶ ‖ , Jean Jaques Hauw ¶ ‖ , Patrick Cozzone § , Didier Dormont ‡†, Jean-Philippe Brandel ¶ , Nicholas Ayache *

Thème ? —
Projet EPIDAURE

Rapport de recherche n° ???? — July 2004 — 55 pages

Abstract: We present a method for the analysis of basal ganglia (including the thalamus) for accurate detection of human spongiform encephalopathy in multisequence MRI of the brain. One common feature of most forms of prion protein infections is the appearance of hyperintensities in the deep grey matter area of the brain in T2-weighted MR images. We employ T1, T2 and Flair-T2 MR sequences for the detection of intensity deviations in the internal nuclei. First, the MR data is registered to a probabilistic atlas and normalised in intensity. Then smoothing is applied with edge enhancement. The segmentation of hyperintensities is performed using a model of the human visual system. For more accurate results, a priori anatomical data from a segmented atlas is employed to refine the registration and remove false positives. The results are robust over the patient data and in accordance to the clinical ground truth. Our method further allows the quantification of intensity distributions in basal ganglia. The caudate nuclei are highlighted as main areas of diagnosis of sporadic Creutzfeldt-Jakob Disease (CJD), in agreement with the histological data. The algorithm permitted to classify the intensities of abnormal signals in sporadic CJD patient FLAIR images with a more significant hypersignal in caudate nuclei (10/10) and putamen (6/10) than in thalami. Using normalised measures of the intensity relations between the

* EPIDAURE Research Project - INRIA, Sophia Antipolis, France
† CNRS UPR640-LENA, Paris, France
‡ Department of Neuroradiology, La Pitié Salpêtrière Hospital, Paris, France
§ CRMBM UMR CNRS 6612, Faculty of Medicine, Marseille, France
¶ INSERM U360, National Reference Cell of Creutzfeldt-Jakob Diseases, La Pitié Salpêtrière Hospital, Paris, France
‖ R. Escourolle Neuropathological Laboratory, La Pitié Salpêtrière Hospital, Paris, France

internal grey nuclei of patients, we robustly differentiate sporadic CJD and new-variant CJD patients, as a first attempt towards an automatic classification tool of human spongiform encephalopathies.

Key-words: Brain MRI, multisequence MRI, grey matter, internal nuclei, Creutzfeldt-Jakob Disease, sporadic CJD, new-variant CJD, image registration, image normalisation, segmentation, human visual system model

Analyse automatique de la distribution des intensités des noyaux gris centraux en IRM multiséquences du cerveau - Application à la maladie de Creutzfeldt-Jakob

Résumé : Nous présentons une nouvelle méthode d'analyse des noyaux gris centraux afin de faciliter le diagnostic des encéphalopathies spongiformes humaines a partir d'IRM cérébrales multiséquences. L'apparition des signaux hyper-intenses au sein des noyaux gris centraux dans les IRM pondérées en T2 est un point commun entre la majorité des formes des maladies à prions. Les séquences IRM T1, T2, et FLAIR-T2 sont utilisées pour la détection des points aberrants dans les noyaux gris centraux. Tout d'abord, les images sont recalées sur un atlas probabiliste et normalisées en intensité. Un filtrage anisotrope est ensuite appliqué afin de préserver les contours. Les signaux hyper-intenses sont extraits par un algorithme qui s'inspire d'un modèle psychovisuel humain. Pour plus de précision, des informations a priori sur l'anatomie issues d'un atlas segmenté permettent d'affiner le recalage et d'éliminer les faux positifs. Les résultats sont robustes et conformes aux observations fournies par les cliniciens. La méthode permet en outre une quantification de la distribution des intensités des noyaux gris centraux. Les noyaux caudés sont désignés comme principales zones d'interêt diagnostic dans la Maladie de Creutzfeldt-Jakob (MCJ) sporadique, conformément aux données histologiques. La méthode a permis, de plus, de classer sans ambiguïté l'intensité des anomalies de signal chez les patients atteints de MCJ sporadique avec un hypersignal FLAIR plus marqué dans les noyaux caudés (10/10) et parfois les putamen (6/10) que dans les thalami. A l'aide de mesures normalisées de relations d'intensité entre les ganglions de la base des patients, nous parvenons à différencier de manière robuste des patients atteints de CJD sporadique et nouvelle variante, ce qui représente une nouvelle approche vers un outil de classification automatique d'encéphalopathies spongiformes humaines.

Mots-clés : IRM du cerveau, IRM multiséquence, substance grise, ganglions de la base, maladie de Creutzfeldt-Jakob, MCJ sporadique, MCJ nouvelle variante, recalage d'images, normalisation, segmentation, modèlle du système visuel humain

Contents

1 Context and Objectives

The identification of early diagnosis markers is a major challenge in the clinical care of patients with Creutzfeldt-Jakob Disease (CJD). This disease raises a number of questions to neuroradiological centres, due to the limited available knowledge that connects it to medical imaging. Some recent studies [4, 13, 18, 44] found strong correspondences between CJD patients and signal activation in the deep grey matter internal nuclei in Magnetic Resonance Imaging (MRI) of the brain. Since CJD is extremely aggressive, detecting the earliest signs of the disease becomes essential in studying its evolution.

This work is completed as part of the GIS-Prions Project, a national project funded by the French Ministry of Health, as a response to the increasing worries regarding the spread and evolution of the Prion protein infection-based diseases. Its goal is to develop techniques for the early detection and classification of various types of CJD, be it sporadic, new variant, genetic or iatrogenic [4, 5]. Besides assisting to better understand the disease evolution, our study aims to improve the early diagnosis of CJD envisaging the application of a prospective treatment. The project involves several research centres across France and a database aiming to include CJD patients from two main neuroradiological centres in Paris and Marseille in the period between April 2002 and April 2004.

1.1 Magnetic Resonance Imaging

Magnetic Resonance Imaging (MRI) has become a leading technique widely used for imaging soft human tissue. Its applications are extended over all parts of the human body and it represents the most common visualisation method of human brain. Images are generated by measuring the behaviour of soft tissue under a magnetic field. Under such conditions, water protons enter a higher energy state when a radio-frequency pulse is applied and this energy is re-emitted when the pulse stops (a property known as resonance) [20]. A coil is used to measure this energy, which is proportional to the quantity of water protons and local biochemical conditions. Thus, different tissues give different intensities in the final MR image. From the brain MRI perspective, this quality makes possible the segmentation of the three main tissue classes within the human skull: grey matter (GM), white matter (WM) and cerebrospinal fluid (CSF). Their accurate segmentation remains a challenging task in a clinical environment.

The relative contrast between brain tissues is not a constant in MR imaging. In most medical imaging applications, little can be done about the appearance of anatomically distinct areas relative to their surroundings. In MRI, the choice of the strength and timing of the radio-frequency pulses, known as the MRI sequence [36], can be employed to highlight some type of tissue or image out another, according to the clinical application. However, the presence of artefacts due to magnetic field inhomogeneity (bias fields) and movement artefacts may hamper the delineation of GM versus WM and CSF and make their depiction difficult.

There is an entire family of MRI sequences that are used in common clinical practice. T1-weighted MRI offers the highest contrast between the brain soft tissues. On the contrary, T2-weighted and Proton Density (PD) images exhibit very low contrast between GM and WM, but high contrast between CSF and brain parenchyma. In other MRI sequences, like the Fluid Attenuated Inversion Recovery (FLAIR) sequence, the CSF is eliminated from the image in an adapted T1 or T2 sequence. More about these specific MRI sequences and their variations can be found in [6]. Multisequence MRI analysis combines the different information provided by the employed sequences. Combining such knowledge gives substantially more information about brain anatomy and possible occurring changes.

MR images depict a 3D volume where the organ or part of the body of interest is embedded. This information can be used to build a 3D representation of the structure of

interest. This applies both to 2D sequences, where images are acquired in slices, and to recently developed 3D sequences, where the data are captured in the 3D Fourier space, rather than each slice being captured separately in the 2D Fourier space [36, 6].

In the next section we will focus on the use of MRI for the detection and classification of Creutzfeldt-Jakob diseases.

1.2 CJD and MRI

MRI is commonly used for non-invasive examinations of patients with neurological diseases. For the last fifteen years, evidence of MRI hypersignals in patients suffering from CJD has been found. However, the observations and studies describing its ability to help in the diagnosis of CJD are in an early stage. Most of the studies are concerned with sporadic CJD cases, which represent 80% of all forms of CJD. The first study cases describe activations in T2-weighted images (and FLAIR T2 images) with higher incidence in the basal ganglia (see Figure 1) in a bilateral symmetric form [15, 27, 32]. Schroeter [34] conducts a large study on sporadic CJD patients and concludes that the MR sensitivity in detecting CJD is 67% with a specificity of 93%. No anomalies are generally reported in T1-weighted images of sporadic CJD patients, with some exceptions, such as in [11].

A great concern in the scientific world has been the occurrence and rapid increase in the number of cases of new-variant CJD in the 1990s, a form of human environmentally-acquired CJD. This type of CJD related to the bovine spongiform encephalopathy shows a different distribution of hyperintensities in brain MRI [29, 43]. In FLAIR and T2 sequences, abnormal high signals are depicted in the thalamus, especially in posterior part of the thalamus or pulvinar nucleus (see Figures 1 and 2). The sensitivity of MRI in diagnosing new-variant CJD is reported as 78% with a specificity of 100%. Unlike the sporadic cases, the new-variants have higher abnormal intensities in the pulvinar when compared to putamen [17]. The caudate, putamen and thalamic nuclei are studied in the neuroradiological diagnosis of new-variant CJD [10].

Other forms of prion infections are genetic, such as Fatal Familial Insomnia (FFI) and Gertsmann-Straussler-Scheinker syndrome (GSS), or iatrogenic CJD, which are much less studied in MR imaging. The rarity of such cases makes them difficult to interpret from a statistical point of view. An overview of the clinical aspects of human spongiform encephalopathies can be found in [4].

Although the intensity of abnormal signals probably changes over time with the evolution of the disease, there are cases where no increase is noted or even no hypersignals appear in the internal nuclei. As mentioned above, cortical hypersignals are also associated with CJD, but on a much more reduced scale. Abnormal cortical signals are best detected in Diffusion Weighted Images (DWI) [2]. Areas of high signal in DWI are usually associated with a decreased apparent diffusion coefficient (ADC) value. Although there are overlaps between bright areas in FLAIR/T2 and in DWI, the MR sequences depict different types of abnormal pathological features.

There are several hypotheses relating hyperintensities in MRI and CJD. In [12, 38], correlation between MRI studies and neuropathological data shows that an elevation of

signal in MRI T2-weighted sequences correlates with gliosis in pathological analysis. In [43, 44] it is also argued that hyperintensities in thalamus related to the variant CJD seem more likely linked to the level of gliosis than to spongiosis or prion deposits. Bahn and Parchi [3] relate the high signal in DWI to spongiform changes. More recently, Haïk et al. [18] noted that, in a sporadic and a variant CJD cases, there is no clear association between the high MRI signal and gliosis or spongiform changes, but seems to be closer related to the accumulation of prion protein. Still, the relation between the prion deposits and strong signal in MRI remains ambiguous.

Despite the given advances in the detection of CJD, to date, clear diagnosis can only be performed post-mortem. In-vivo pathological examinations could rarely be carried out through brain biopsy to confirm the diagnosis of CJD. However, brain biopsy is a risky invasive procedure with far from perfect results, since it is dependent on the brain sampling area. Through recent advances in the description of MRI abnormalities related to CJD, MRI is considered an essential tool in CJD diagnosis.[14, 27, 28] make MR related image processing an important tool in non-invasive CJD diagnosis. However, the interpretation of MR images is usually limited to a visual inspection performed by the medical staff and could lead to an under- or overestimation of the true incidence of CJD [5]. At present time, MRI is not included as a diagnosis criterion for sporadic CJD, although, as argued in our results and discussion sections, it presents valuable information to the clinician. It would be certainly useful to include MRI in the diagnosis of sporadic CJD, as for the variant forms [44]. Therefore, the necessity to further explore the advantages of Computer Aided Diagnosis (CAD) techniques in the MRI clinical environment becomes obvious.

Leemput [39] proposes a method for automated quantification of MR intensity changes in images of patients suffering from CJD. He acknowledges as common difficulties in processing such images the limited resolution, partial volume effects, noise, low contrast and intensity inhomogeneities, whether this is performed by the computer or the human expert. Hence, low level segmentation methods are inappropriate for the detection of hyperintensities in the affected areas of the brain. A mixture model of normal distributions combined with the expectation-maximisation algorithm (EM) is proposed. However, the method does not detect signal abnormalities in most of the CJD cases, while showing significant amounts of false positives (FP) along the interface between grey matter (GM) and cerebrospinal fluid (CSF).

Hojjat *et al.* analyse the putamen intensity gradient [19] in a series of sporadic and new-variant CJD patients. They discriminate new-variant from sporadic and new-variant from normal cases using T2-weighted and Proton Density MRI, but cannot separate sporadic CJD patients from controls. Their segmentation of putamen is performed manually prior to the intensity analysis.

1.3 Addressing the Problem

Little is known about the early evolution of CJD patients. Most of the studied cases are of patients severely affected by the disease, as there is poor evidence of Prion infection at an early stage of the disease. Early detection of CJD is essential for better understanding of

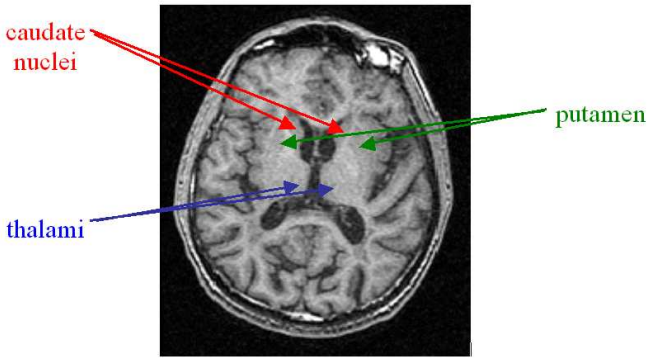

Figure 1: A map of deep grey matter internal nuclei in a normal T1 weighted axial MR image. The red arrows point towards the caudate nuclei, while blue and green arrows indicate the thalami and the putamen respectively.

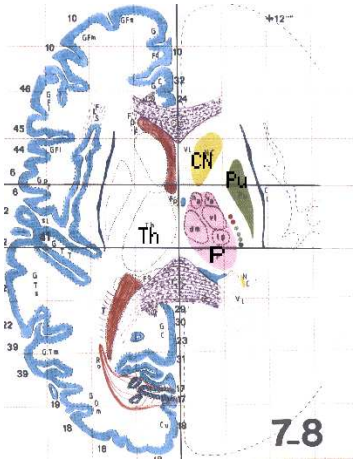

Figure 2: A map of deep grey matter internal nuclei reproduced from Talairach and Tournoux atlas [37]. The caudate nuclei (CN) are shown in yellow, the putamen (Pu) in green and the thalami (Th) in magenta. The pulvinar (P) is located in the posterior section of the thalamus

this lethal disease and for a shorter path towards finding its treatment. Likewise, little is known about possible ways to visualise and represent signs of CJD in conventional medical imaging.

Computer Assisted Diagnosis (CAD) algorithms have been introduced in clinical settings and automatic computerised methods to assist clinicians in detecting and characterising diseases are being developed. Their utility in a large number of clinical applications has been proven by multiple studies. They simplify the complex laborious tasks of every day clinical work, assist in the routine of investigating large numbers of medical images (which makes the human factor prone to errors) and present a valuable second opinion in decision making. Given the present knowledge and limitations in analysing medical images, namely MRI of the brain, for CJD related applications, we aim to detect Prion infections at an early stage and with the requested robustness and reliability desired in clinical applications.

The motion artefacts found in the set of images we work with (exemplified in Section 4) makes the use of statistical detection algorithms very difficult. Such algorithms rely on finding consistent repeatable signs of a disease over a set of patients [22, 23, 40]. Also, they need good contrast between GM and WM in T1-weighted images for stochastic analysis according to a general atlas context. This is another major source of errors in cases of CJD, where patients suffer of severe dementia with often uncontrolled movements. In Figure 10 we note the contrast between soft brain tissues in a typical T1 image versus a typical T1 of a patient suffering from CJD.

The approach we propose is based on the use of a priori anatomical knowledge in the form of an accurately segmented and labelled image (e.g. the Zubal Atlas [45]) for precise segmentation and of a probabilistic atlas for intra- and inter-patient analysis. A feature detection technique based on a model of the Human Visual System (HVS) is employed for the depiction of hyper-signals. The remaining of this paper is organised as follows: Section 2 presents the complex pre-processing steps applied to the input images before the effective segmentation of disease activations. This includes spatial and intensity normalisation, atlas alignment and noise removal by anisotropic diffusion. Section 3 introduces the refined registration of internal nuclei using a segmentation atlas. Then we present the HVS-based detector, an adaptive thresholding method following the functioning of the human eye, that is used to segment abnormalities in deep grey matter. Some results of our method are illustrated in Section 4, before discussions and conclusion in Section 5.

2 Pre-Processing

In this section we will review the pre-processing stages used before the actual segmentation of CJD hypersignals. This is a simplified model of data normalisation and regularisation, which is required to put the images in the same general framework. The main advantage of image normalisation is the drastic reduction of the number of parameters. We further expand on these steps.

2.1 Data

The image acquisition protocol is designed to include three MRI sequences for each patient. As mentioned above, we can extract different kinds of information from each sequence relevant to our application. The sequences used by our algorithm are: a T1-weighted acquisition for its higher contrast between GM and WM and higher image resolution; T2-weighted images for the good contrast between the CSF and the brain parenchyma; and a T2-weighted FLAIR sequence, well-established for the depiction of CJD related activation in the brain. We use the T1 sequence to find the first estimate of the transformation for the registration process, the T2 for segmentation of CSF and brain and the FLAIR for segmentation of bright abnormalities in basal ganglia.

2.2 Image Normalisation

The large variability inherent to human anatomy and imaging parameters leads us to consider spatial and intensity normalisation as an approach to normalise patient images for further abnormality detection. This is done both for localising the areas of interest with the help of an atlas of the brain, but also for normalising specific imaging parameters for an automatic detection of the affected brain areas. Furthermore, inter-patient analysis could now be performed.

2.2.1 Spatial Normalisation

Data registration to an atlas has become a common technique with the introduction of popular statistical algorithms for image processing, such as Statistical Parametric Mapping (SPM) [1] or Expectation Maximization Segmentation (EMS) [40]. A well-known probabilistic atlas in the scientific community is the MNI Atlas from the Montreal Neurological Institute at McGill University [9]. It was built using over 300 MRI scans of healthy individuals to compute an average brain MR image, the MNI template, which is now the standard template of SPM and the International Consortium for Brain Mapping [26]. The averaging is performed for the entire brain, but also on isolated GM, WM and CSF, providing a tool for statistical segmentation. For these reasons, we chose the MNI template as the basis for image alignment in our approach. Figure 3 shows the MNI template.

We propose the following registration scheme. T1 images have the highest resolution in our data set, hence we register them to the MNI template first using an affine transformation. The registration algorithm, previously developed in our group, is described in [31]. It uses a block matching strategy in a two-step iterative method. The standard assumption behind the algorithm is that there is a global intensity relationship between the template image and the one being registered to it. The method proposes several types of correlation measures: linear, functional or statistical. Using one of these, the correlation coefficient in our case, the transformation between the two images is computed block by block and a displacement field is thus generated. A parametric transformation, either affine or rigid, is then estimated

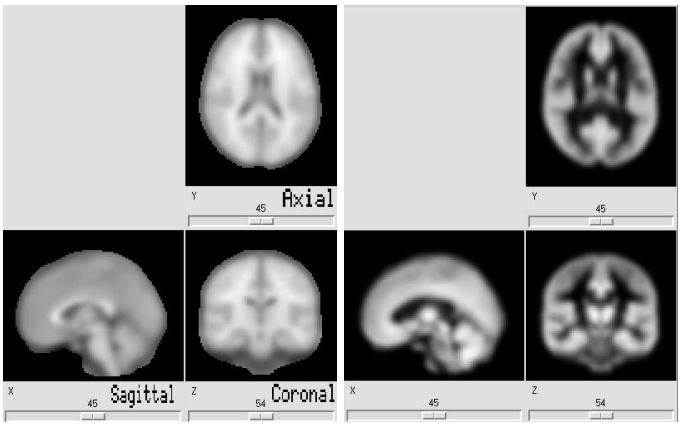

Figure 3: The MNI template. On the left, the probabilistic MNI atlas of the brain; on the right, the corresponding GM atlas. Please note the arrangement of MR images in radiological convention with an axial, a sagittal and a coronal view. This convention is reflected in figures throughout the paper.

from this deformation field. To further improve robustness, this procedure is repeated at multiple scales. More details can be found in [30].

Next, rigid intra-patient registration of all sequences is performed using the same algorithm as above. Both the T2 and the FLAIR images are registered to the T1 image. By combining this rigid transformations with the affine transformation matching T1 and MNI template, we can find correspondences between the atlas and the T2 and FLAIR images. This is illustrated in Figure 5. The final image resolution is that of the MNI atlas: 91x109x91 voxels. Figure 4 shows an example of spatial normalisation. With all images registered to the atlas, intra- and inter-patient analysis becomes simple and statistical algorithms can be applied.

2.2.2 Intensity Normalisation

In addition to geometric variability, MR images may also exhibit intensity variations. Contrast differences over a set of images are a common problem in image analysis. One can note considerable variations between images of different patients, but also in images of the same patient taken at different times. This makes identical anatomical parts of the imaged area appear with different intensities from one image to the next. As a result, it is difficult to tune processing parameters for robust repeatable results. To overcome problems, we propose the use of an intensity normalisation algorithm for the FLAIR images, prior to the detection of signal deviations. Our method performs an affine equalisation using the joint histogram

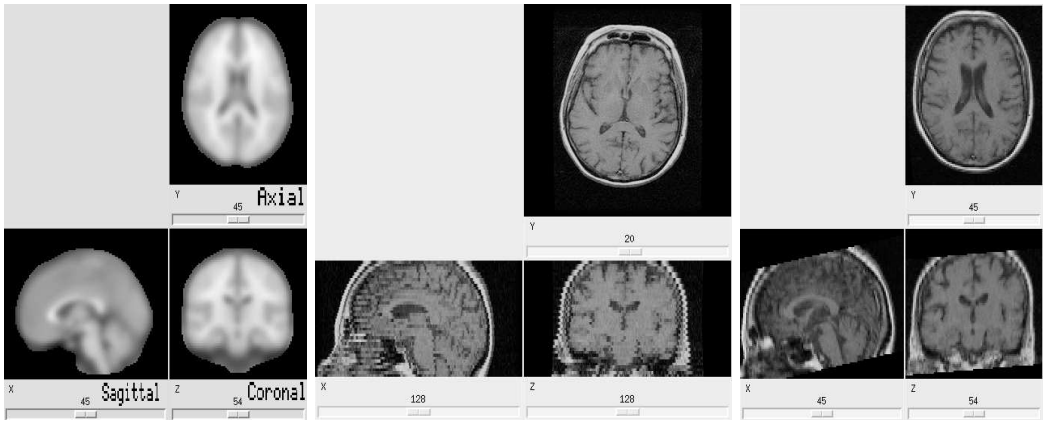

Figure 4: An example of spatial normalisation. The image on left shows the MNI template; the middle image is the subject's T1 before registration; the right image is the subject's T1 after spatial normalisation.

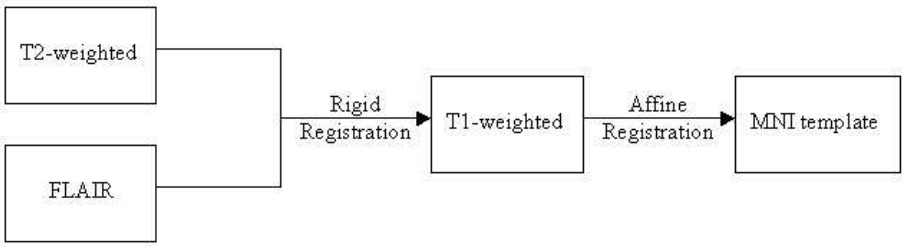

Figure 5: Diagram of the spatial normalisation algorithm. Intra-patient images are rigidly registered on the corresponding T1. The T1-weighted image is affinely registered to the atlas template. The resulting transformation is used to align all other MR images to the atlas.

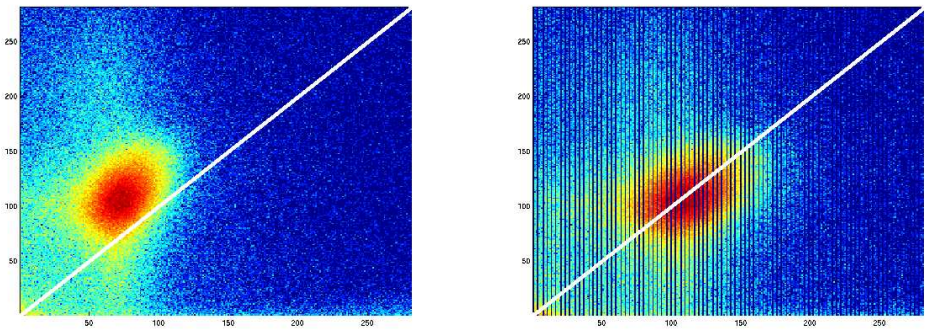

Figure 6: The joint histograms of the two MR patient images in Figure 7 before intensity normalisation (left) and after the affine regularisation of intensities (right). We note the realignment of the cloud of points in the middle of images to fit better the first diagonal (shown in white) once the image normalisation has been performed. The dark lines appearing in histogram of normalised images are caused by the dilation of the range of values in the image to be normalised; as we work with discrete data and we do not employ any interpolation, the affine normalisation will not cover the entire range between the minimum and maximum values leading to this visual artefact.

of two images: a standard image onto which we align the intensity distribution of a second input image [33].

The two images must be registered prior to normalisation in intensity to align anatomical coordinates for the best use of the joint histogram between the two images. Ideally, the joint histogram will be as close as possible to a straight line along the first diagonal of the intensity plane, which is the result we aim to achieve with the affine intensity equalisation. In practice, a joint histogram between MR images of different subjects following the same acquisition protocol looks like a cloud of points centered around a line ($I_2 = aI_1 + b$) in the intensity surface. The affine equalisation we employ finds the parameters a and b by minimising the criterion C in equation 1, where i relates to the points of coordinates (I_{1i}, I_{2i}). Figure 7 shows an example of intensity normalisation between the MR images of two patients. Next in Figure 6 we can note the change in the joint histogram of the images shown in 7 before and after intensity normalisation.

$$C = \sum_i \frac{|I_{2i} - (a + bI_{1i})|}{\sqrt{1 + b^2}} \tag{1}$$

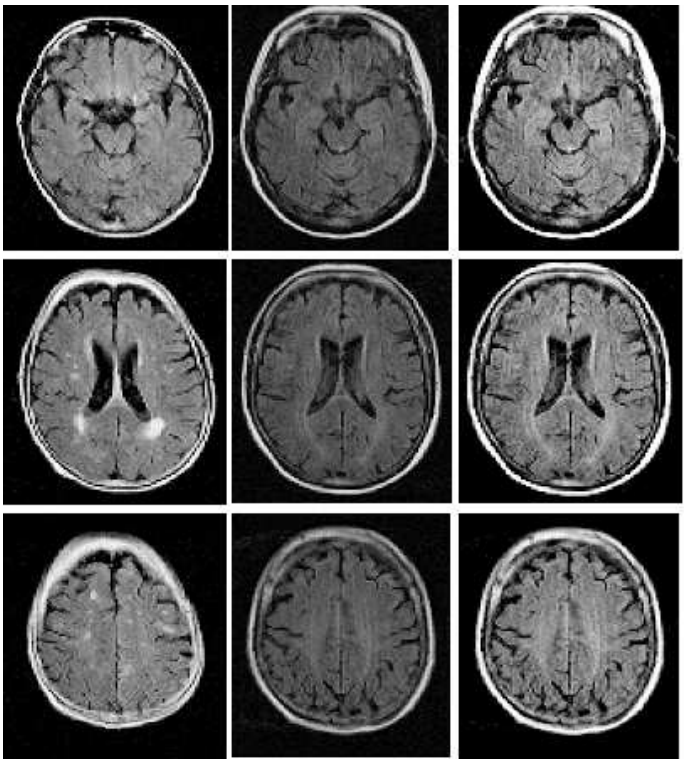

Figure 7: An example of intensity normalisation on FLAIR images. On the left column, three axial MR cross-sections of the first subject are shown; in the middle are the cross-sections of the second subject before normalisation; on the right column are the cross-sections of the second subject normalised in intensity with respect to the first subject.

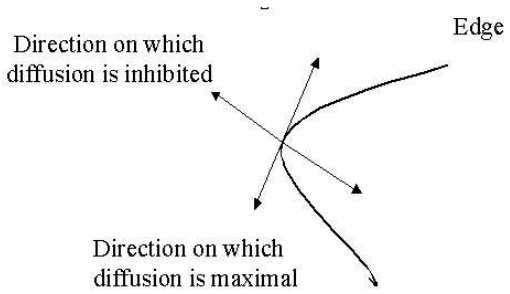

Figure 8: The anisotropic diffusion eigenvectors of the diffusion tensor. Smoothing is allowed along the edge, while inhibited across the margin.

2.3 Noise Removal and Image Enhancement

MR images are noisy. Our application aims to detect areas of abnormal intensity in the deep grey matter of the brain and noise can hamper the segmentation process. Thus, it seems natural to smooth our images in order to remove unwanted noise. However, we must ensure that the areas of interest (areas of high intensity) are preserved for accurate segmentation. Therefore, an edge-preserving blurring technique is required. Anisotropic diffusion offers the tool to perform image smoothing with edge enhancement, as our application necessitates. Figure 8 illustrates the direction of maximal and minimal diffusion of the nonlinear anisotropic diffusion model introduced by Weickert [41]. This model uses a diffusion tensor with has two orthonormal eigenvectors (instead of a diffusivity function) that determine the direction of diffusion. Smoothing will take place along edges, but will be inhibited across boundaries. The choice of related eigenvalues determines the behaviour of the feature detector. We employ a strong decreasing diffusivity-like function that encourages strong smoothing within contours, while contrast at edges is enhanced. Equation 2 shows the eigenvalue (λ) corresponding to the eigenvector across the edge, where I is the image to diffuse.

$$\lambda = \begin{cases} 1 & |\nabla I_\sigma| = 0, \\ 1 - \exp\left(\frac{-1}{(|\nabla I_\sigma|/k)^{12}}\right) & |\nabla I_\sigma| > 0 \end{cases} \tag{2}$$

A few parameters are involved in the diffusion process, namely the scale of the Gaussian used to smooth at each iteration (σ), the number of iterations over which smoothing is done (t) and the contrast (k) which determines the presence of an edge. We employ a kernel for the Gaussian of size 5x5 (to smooth only small areas in images that have already small resolution) over 5 iterations, when the contrast approximates the mean of the image gradient (to ensure the stability of more significant edges in the image). We show an example of image

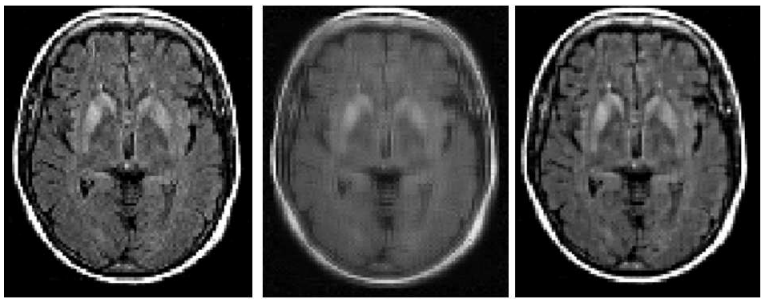

Figure 9: The effect of anisotropic versus linear diffusion on image smoothing. On the left, we show the original image from a patient with typical CJD activations in the basal ganglia; in the middle, the linearly diffused (Gaussian convolution) image after 5 iterations; on the right,the anisotropically diffused image after 5 iterations with smooth areas and well-preserved edges.

diffusion in Figure 9. After diffusion, images have a better Signal-to-Noise Ratio (SNR) and small registration errors are also corrected.

3 Segmentation and Refined Registration

Our analysis is based on the abnormal MR intensities that can appear in the basal ganglia (including the thalamus) of patients suffering from CJD. To be able to segment GM and WM in MRI sequences, a good contrast between these types of tissues in T1-weighted images is desired. Figure 10 shows a typical T1 with high contrast between brain's soft tissues and a common T1 image from our database. Under the given circumstances, the segmentation of GM (where CJD affections are visible) cannot be done directly from the patient images. The MNI atlas can provide a probabilistic segmentation of GM, but this is not precise enough for our application. We use instead a segmented anatomical atlas of the brain, the Zubal Phantom [45], which is introduced in the next section.

3.1 A Priori Anatomical Data

The data we use were affinely registered to the MNI atlas. While we avoid direct non-rigid registration, which may induce large interpolations and alter the MR intensities, the affine registration is only approximate. A precise local intensity analysis of internal nuclei would be erroneous at this stage (see Figure 16) and therefore a registration refinement becomes necessary. The Zubal atlas offers a precisely labelled segmentation of brain structures from the T1-weighted MR image of one single subject. Our interest focuses on the internal nuclei, which are segmented in the phantom. First, the atlas must be aligned to our set of

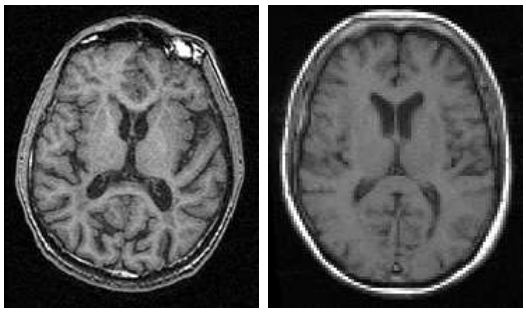

Figure 10: A typical T1-weighted MR image with good contrast between brain GM, WM and CSF (left) versus a T1 image from our data set (right).

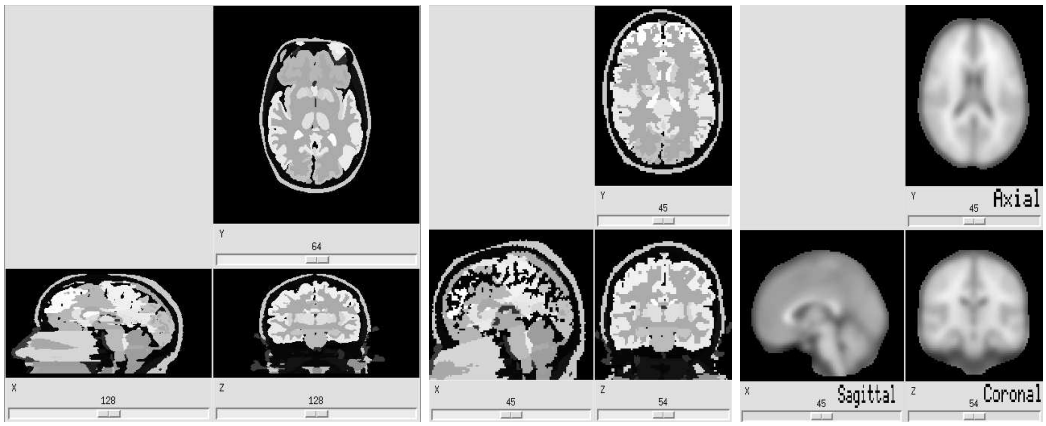

Figure 11: The registration of Zubal Phantom onto the MNI template. On the right, the original Zubal Phantom is shown; in the middle, we have the registered Zubal Phantom on the MNI template, which is shown in the right image.

images, which have been previously registered to the MNI atlas. Thus, we register the Zubal Phantom to the MNI template, again using our block matching algorithm [31], to estimate an affine transformation. However, in order to preserve the correct values of the segmentation labels posterior to the application of the transformation, nearest-neighbour interpolation is performed, as opposed to the case of patient image registration, which employed spline interpolation. Figure 11 shows the results of registering the Zubal Phantom to the MNI reference without disrupting the Zubal labels.

3.2 Detection of Internal Nuclei and Refined Segmentation

Once the Zubal Phantom is registered to the working framework, we can easily depict the brain structures that are of interest, namely the deep GM internal nuclei. Reports in the literature [4, 13, 18, 43, 44] mention the importance of analysing MR intensities in the basal ganglia. Hence, we create a mask with the thalamus, putamen and head of the caudate - which will be referred as internal nuclei for the rest of this paper - from the Zubal Phantom registered on MNI (Figure 12). We aim to use this mask for the segmentation of internal nuclei in patient images. Although the affine registration gives correct correspondences in a general brain registration framework, the anatomical variability between patients makes the correspondence between the Zubal internal nuclei mask and the corresponding internal nuclei in each patient erroneous. A refinement of the registration in the deep GM between the Zubal internal nuclei mask and the patient internal nuclei seems necessary to allow us to use the a priori anatomical information resulting from the segmentation of the Zubal Phantom.

The segmentation of internal nuclei in patient images is not an obvious task; this is why we exploit the Zubal Phantom. Nevertheless, there are other important anatomical landmarks in the brain that are easier to identify. We concentrate on the segmentation of ventricles and cortex external boundary. Ventricles will give a good approximation of the deformation field around the internal nuclei, whereas the cortex boundary will impose the global spatial correspondence and stabilise the deformation field inside the brain. Figure 12 illustrates the segmentation of ventricles, brain contour and internal nuclei from the registered Zubal Phantom.

To obtain similar images of segmented brain margin and ventricles for each patient, we employ morphological opening on patient T2 images. The strong contrast that CSF has against the brain in T2-weighted images allows us to segment the ventricles, while the cortex boundary can be extracted from either T1 or T2 sequences. We prefer using the T1 sequence, since the T2 image we employ lacks some top and bottom slices. The ventricles being located in the middle of the brain, it is correct to extract them from T2 images, but the cortex would be incomplete. We now are in the possession of two binary maps of ventricles and brain boundaries for each patient: one from the Zubal Phantom and the other from the patient. Non-rigid registration is used to align the two images, employing the algorithm described in [7]. Figure 13 shows typical results and Figure 14 shows the 3D deformation fields related to the registration in Figure 13. The outer margin of the cortex ensures that the deformation fields are spatially sound and do not pull the internal nuclei over their location.

Having the deformation fields computed, we apply them to the mask of internal nuclei of the Zubal Phantom, deforming the mask according to the position and size of the ventricles in the patient image. A diagram of the algorithm is shown in Figure 15. The deformed mask is used to segment the internal nuclei of the patient, mainly the putamen, head of the caudate and thalamus, areas associated with strong signals in the diagnosis of CJD. Figure 16 shows an example of registration of internal nuclei in 3D and the internal nuclei segmentation results in a T1-weighted MR image of a patient. A segmentation of internal

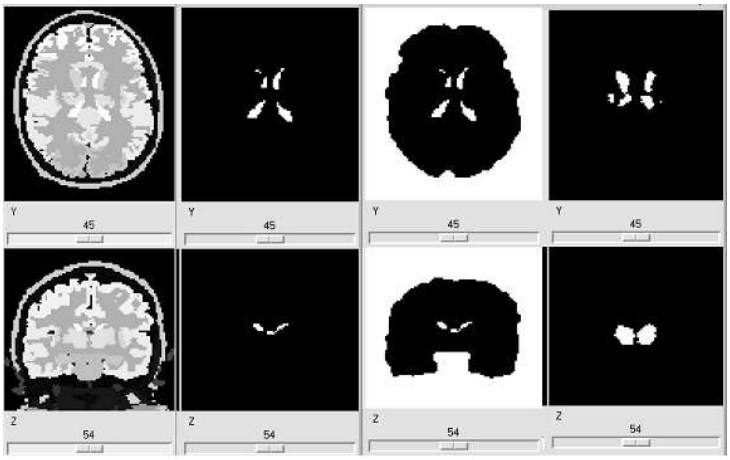

Figure 12: The segmentation of the Zubal Phantom. From left to right: column 1, the Zubal Phantom registered on MNI; column 2, the ventricles segmented from the Zubal Phantom; column 3, the cortex outer boundary is added to the ventricles; column 4, the internal nuclei segmented from the Zubal Phantom.

nuclei is essential in discarding possible false positives in the detection of hyperintensities. In Figure 17 we show more details about the segmentation of internal nuclei by browsing through the MR slices (i.e. axial, coronal and sagittal) of a patient. More will be presented about it in the results section.

3.3 Human Visual System

The detection of areas of CJD activation in the brain is completed by a foveal segmentation algorithm. This is in essence a method of adaptive thresholding, which uses a mathematical model of human vision. Its motivation comes from the better sensitivity and specificity that the human eye has over classical algorithms in detecting and characterising image features. Figure 18 shows the variation of the threshold C_{min} adopted in our model over the variations in image intensity. $C_{classic}$ represented a classical non-adaptive threshold. A simplified model for the computation of C_{min} is shown in equation 3, where c_{mpc} is the minimal perceivable contrast, b is constant, μ_N the mean value of the intensity of neighbourhood and μ_A a mean weighted value of neighbourhood and background (entire image). The model is presented in greater detail in [25].

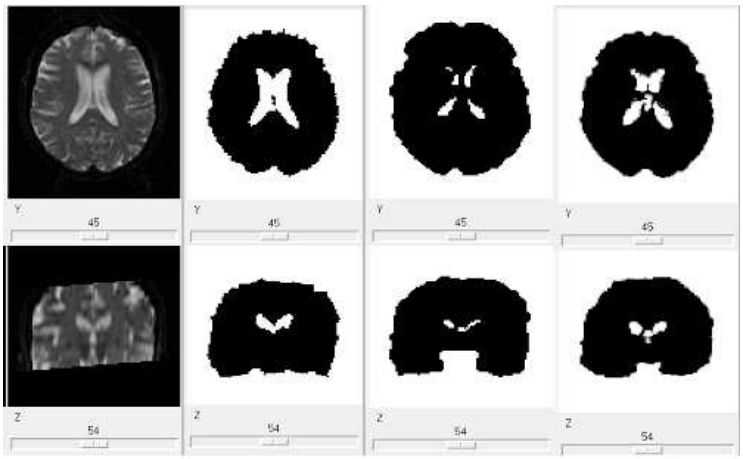

Figure 13: Registration of the Zubal ventricle and cortex outer boundary on a patient with very large ventricles. This is the most difficult case encountered, due to the patient's brain atrophy and the significant dilation of ventricles, next to the small ventricles in the Zubal Phantom, where the subject is young. The algorithm gives robust results, as seen above. From left to right: column 1, the T2 image of the patient registered on MNI; column 2, the ventricles and brain margin of the patient (ventricles segmented from T2 and cortex from T1); column3, the ventricles and brain boundary of Zubal Phantom; column 4, the ventricles and cortex boundary of the Zubal Phantom registered on the patient.

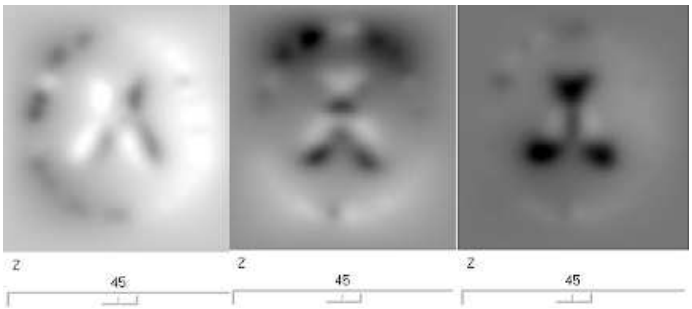

Figure 14: Deformation fields of the non-rigid registration between the Zubal Phantom ventricles and those of a patient with very large ventricles. On the left is the x field, the y field is in the middle column and the z field on the right.

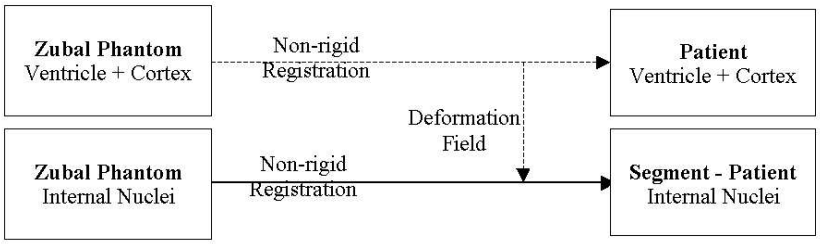

Figure 15: Diagram of the refined registration of internal nuclei.

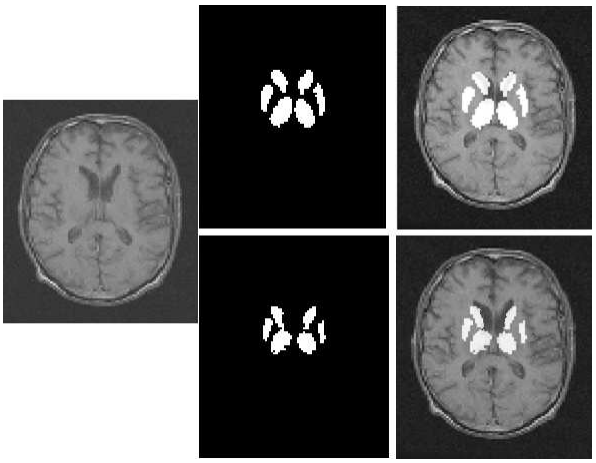

Figure 16: An example of internal nuclei registration and their segmentation in a T1-weighted image of the patient. On the left, we have the T1 image of the patient; in the middle column the internal nuclei maps; on the right, we show the segmentation of internal nuclei according to the binary map. The rows show: top - before non-rigid deformation with the head of the caudate superposed on the ventricles, bottom - after non-rigid deformation, showing an accurate segmentation.

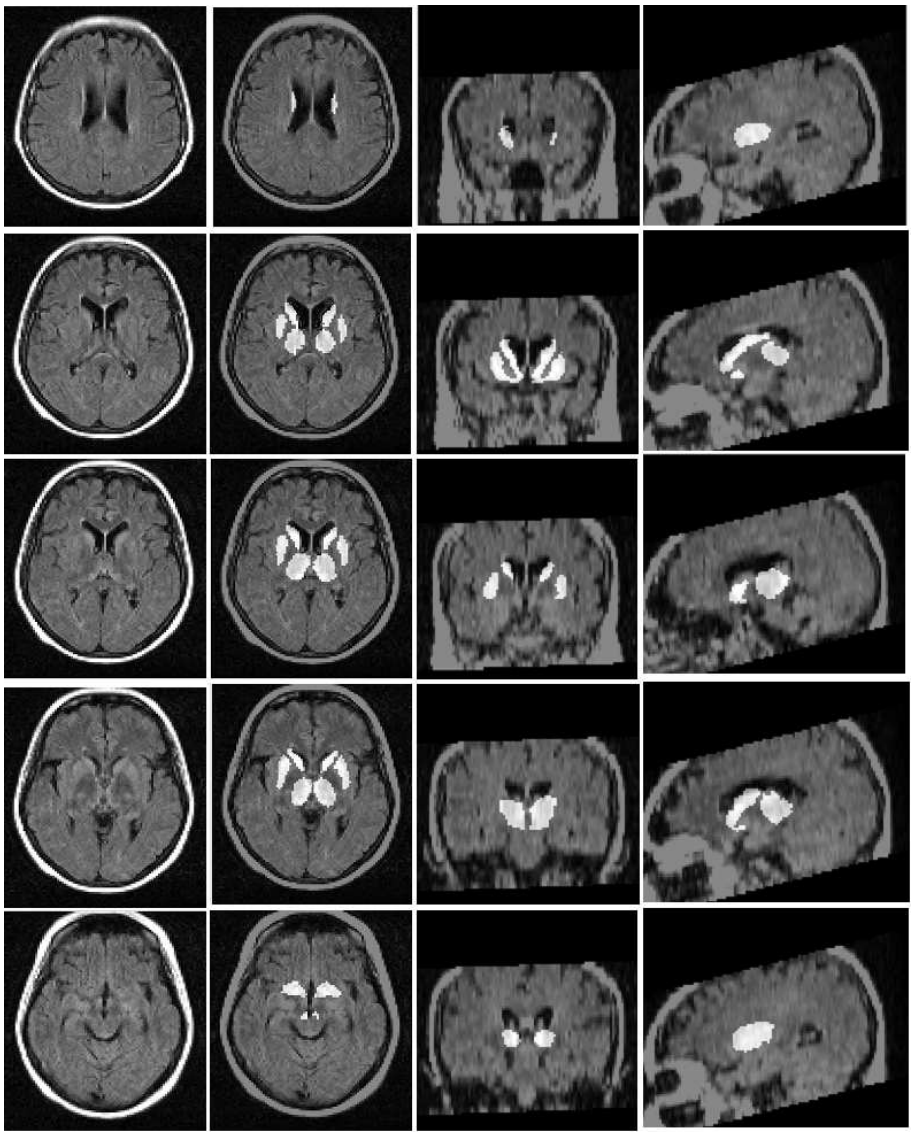

Figure 17: Another example of internal nuclei registration and their segmentation in a T1-weighted image of the patient. In the far left column, we present the axial T1 slices of the patient; in the inner left column the segmentation of internal nuclei in the corresponding axial slices; in the inner right column, we have the segmentation of internal nuclei in coronal MR slice; while in the far right column we show the segmentation results in sagittal MR slices.

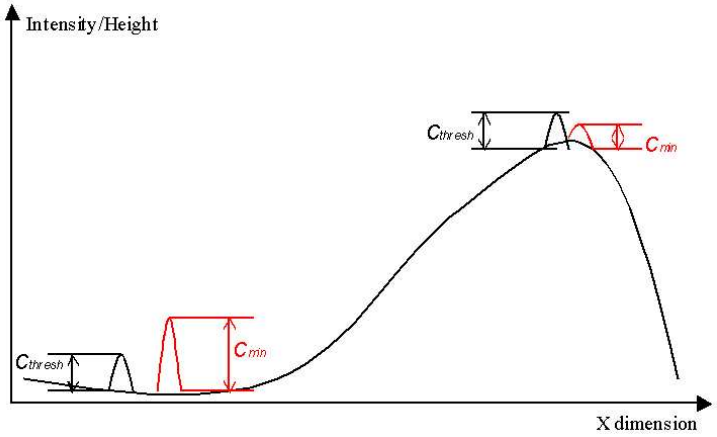

Figure 18: The adaptive qualities of the HVS model. The threshold C_{min}changes according to the values in its immediate neighbourhood and the mean intensity of the image.

$$C_{min} = \frac{c_{mpc}}{\mu_N} \left(b + \sqrt{\frac{\mu_N^2}{\mu_A}} \right)^2 \tag{3}$$

There are a number of parameters involved at this stage. Relevant for our application are the size of the fovea and the minimal perceivable contrast of the human visual system (HVS) model. Empirically, we noted that activations in deep grey matter are not very small, as they usually involve a significant surface of the putamen, head of caudate or thalamus. We set the size of the kernel of fovea to 15x15 pixels to be able detect small enough areas of hyperintensity, but large enough not to depict high frequency noise. As argued in [25], the minimal perceivable contrast must be computed as a function of the image gradient in order to accommodate all possible variations of contrast. In MR images of the brain, the intensity values of GM, WM and CSF can be regularised by intensity normalisation. Therefore, hyperintensities can be regarded as an exception to the normal intensity distribution. In this particular case, the minimal perceivable contrast can be constant over the whole collection of images.

Pending on image quality and movement artefacts, there will still exist some contrast variability especially between GM and WM and from one image to another. Using an adaptive contrast measure both locally and globally, through the HVS foveal segmentation, our algorithm is less sensitive to such artefacts and image quality and depicts more precisely the abnormal intensity distributions in GM.

4 Results

The data collected for the GIS-Prions Project was acquired in two major neuroradiological centres of France: the Pitié-Salpêtrière Hospital in Paris and the Timone Hospital in Marseille. The databases comprise a total number of 21 MR images: 10 sporadic CJD cases, 3 new-variant CJD cases and 8 normal controls. The ages of patients vary between 31 and 79 years, with an outlier of 18 years and an average age of 55.61 years. The ages of controls vary between 31 and 68 with an average age of 51.87 years. In the first two subsections we present the two databases along with results of hyperintensity detection. Subsequently we introduce the Intensity Quantification Study (IQS). The MR scanner used in the two neuroradiological centres being from different manufactures and the acquisition protocols slightly different, in a first instance we treat the two datasets differently for the presentation of quantitative results, before addressing them in a common normalised framework.

We focus on the three groups of deep grey nuclei: thalamus, putamen and caudate nuclei, for the detection and quantification of hypersignals. Hyperintensities may be present in several subthalamic nuclei (see the "hockey stick" abnormal intensities in new-variant CJD patients in Figure 22) and we show detection results in the entire thalamus. However, previous clinical studies highlighted the relevance of pulvinar (the posterior part of thalamus) in the CJD diagnosis, and we demonstrate the utility of quantifying the pulvinar hyperintensities in the classification of CJD.

4.1 Paris Data

In this first part of the section, we show examples of detection of abnormal hyperintensities in FLAIR MRI on images from patients suffering from CJD collected at the Pitié-Salpêtrière Hospital in Paris. We use T1-weighted (TE=20, TR=500), T2-weighted (TE=92, TR=3000) and FLAIR-T2 (TE=148.5, TR=10002, TI=2200) MR images acquired using a GE Signa scanner. Our database comprises 10 patient specific images with probable CJD-related prion infection: 6 sporadic CJD, 3 new-variant CJD and 5 normal controls. Histological exams are available for all three new-variant CJD patients and only three of the sporadic CJD cases. For each patient we have a T1-weighted, a T2-weighted and a T2 FLAIR sequence. In the examples shown below, we used all three MR imaging sequences for the registration of images and segmentation of hyperintensities. Except for the three new-variant patients, diffusion tensor MR images (DTI) are also available for the rest of the database. A review of the different stages of our algorithm is shown in Figure 19.

The main areas of interest in CJD are the basal ganglia. Using the mask of internal nuclei, we focused on these structures and did not take into account signal abnormalities in other brain regions, such as white matter high signals that are known to correlate with age and vascular risk factors.

Figures 20 and 21 show detection results on six patients suffering from sporadic CJD. The diagnosis is confirmed by histological examinations in three of the cases. The main radiological characteristic of sporadic forms of CJD diseases is the presence of higher intensities in the caudate nuclei and putamen, while the thalami are less, if at all, affected. Visually,

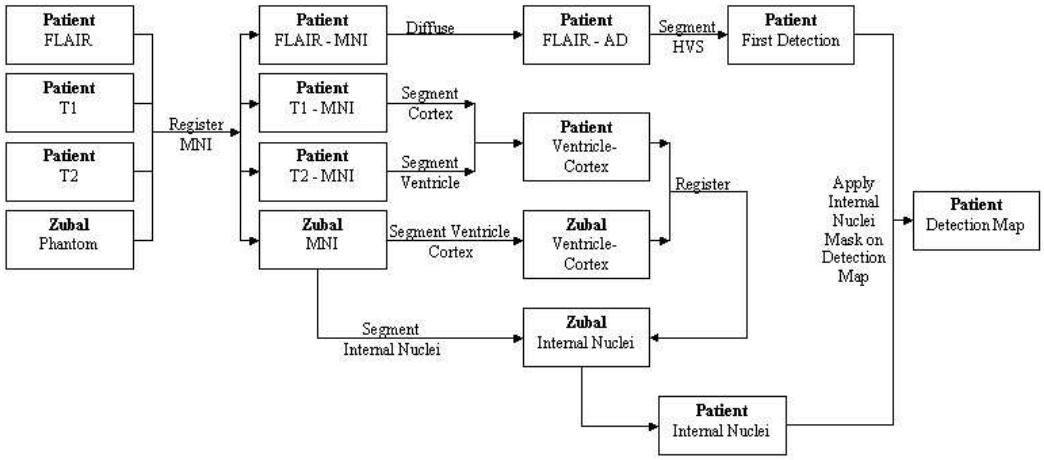

Figure 19: Flowchart of the algorithm proposed for the detection of CJD-related abnormal hyperintensities in multisequence MRI of the brain.

the first two patients presented in each of the Figures 20 and 21 comply to this general rule, while the third respective patient in each figure has high intensities (in yellow and red) in the thalami as well. Also, we note the asymmetry of high signals in the second two cases in Figure 20.

The detection of hyperintensities in new-variant CJD cases is further shown in Figure 22. The thalamic abnormal intensity distributions are present in all these cases and their high intensities are comparable to those detected in putamen and caudate nuclei. Sporadic cases may also show evidence of pulvinar hyperintensities and they can mimic new-variant cases [18], but these intensities are lower in magnitude when referred to the caudate and putamen intensities. The most affected subthalamic nucleus is the pulvinar and we note that hyperintensities do not spread all over the thalamus and are localised in the posterior and dorsomedial thalamic areas, which gives the "hockey-stick" appearance of the hypersignals, as in Figure 22.

The data from Paris includes five normal controls and the results of our algorithm on these images are shown in Figure 23. While no abnormal intensities are depicted in the first four images (top row in Figure 23), a motion artefact leads to a false positive (FP) in the third control image. The artefact lays within the left thalamus, but outside the pulvinar area.

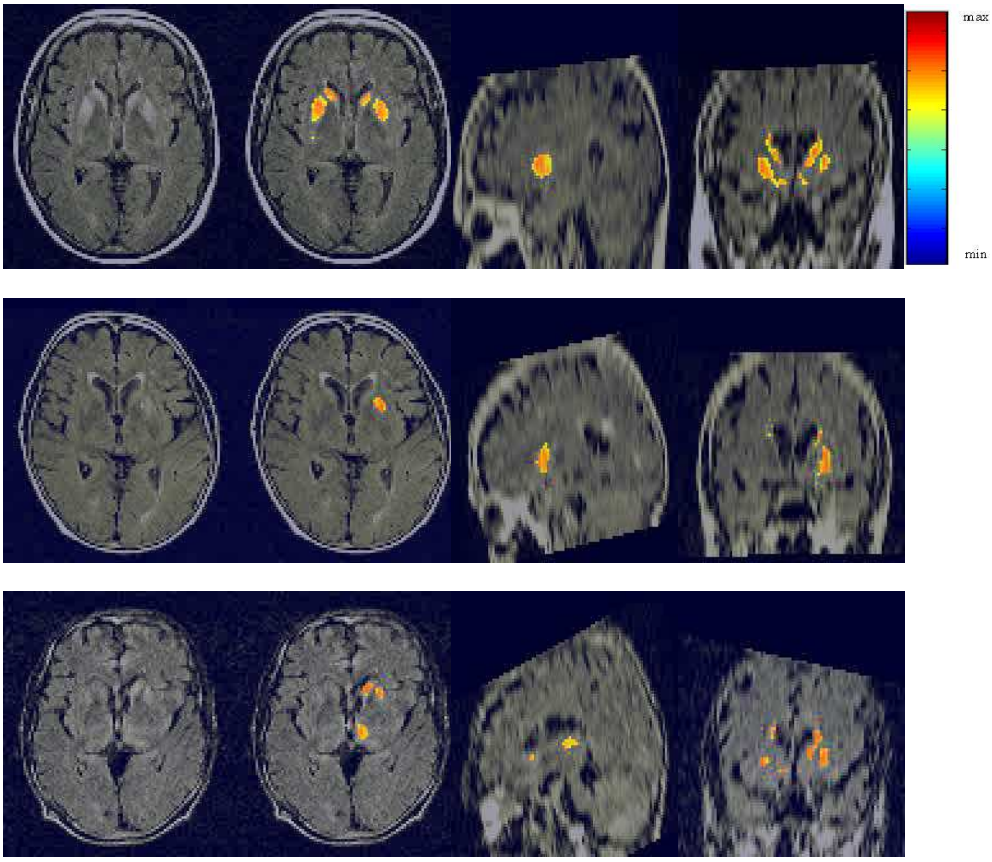

Figure 20: Results on patient data - part I. All three sets of images reported above (one row by case) originate from patients with histologically proven sporadic CJD. We present on the left a cross-section of the FLAIR MR data with abnormal hyperintensities in the internal nuclei; next to it we have the CJD detection map with corresponding intensities, as seen in the attached colourmap; further to the right, we present a sagittal cross-section and a coronal cross-section with their detection maps.

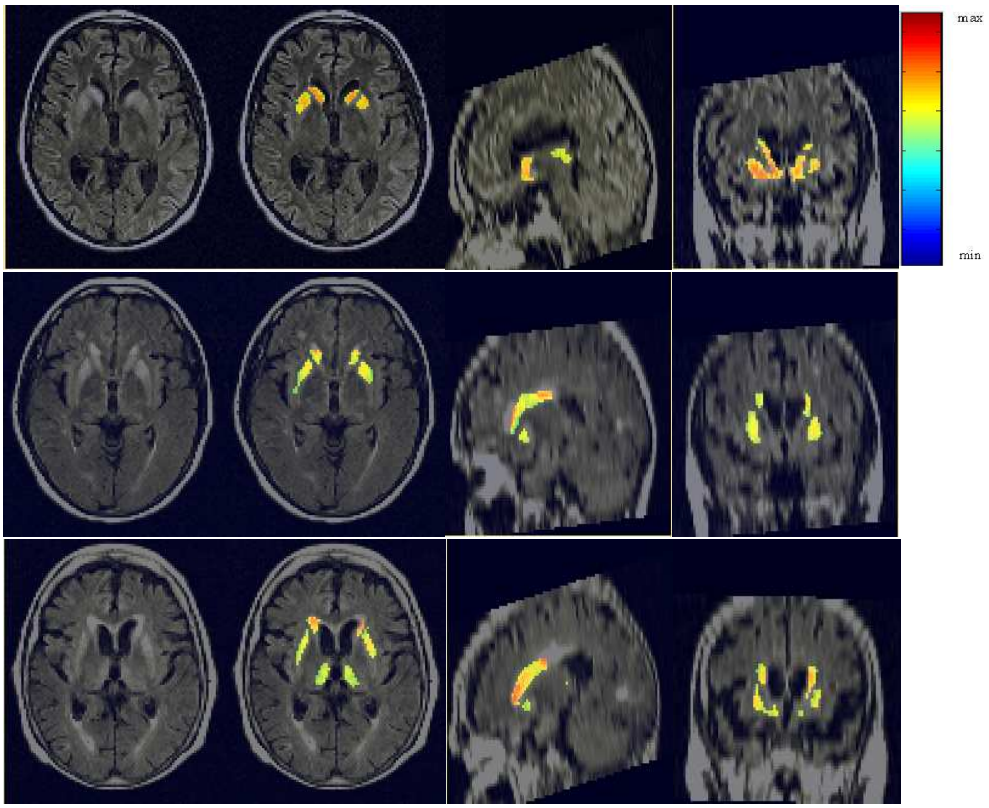

Figure 21: Results on patient data - part II. All three sets of images reported above (one row by case) originate from patients with probable sporadic CJD)no histological examination available).

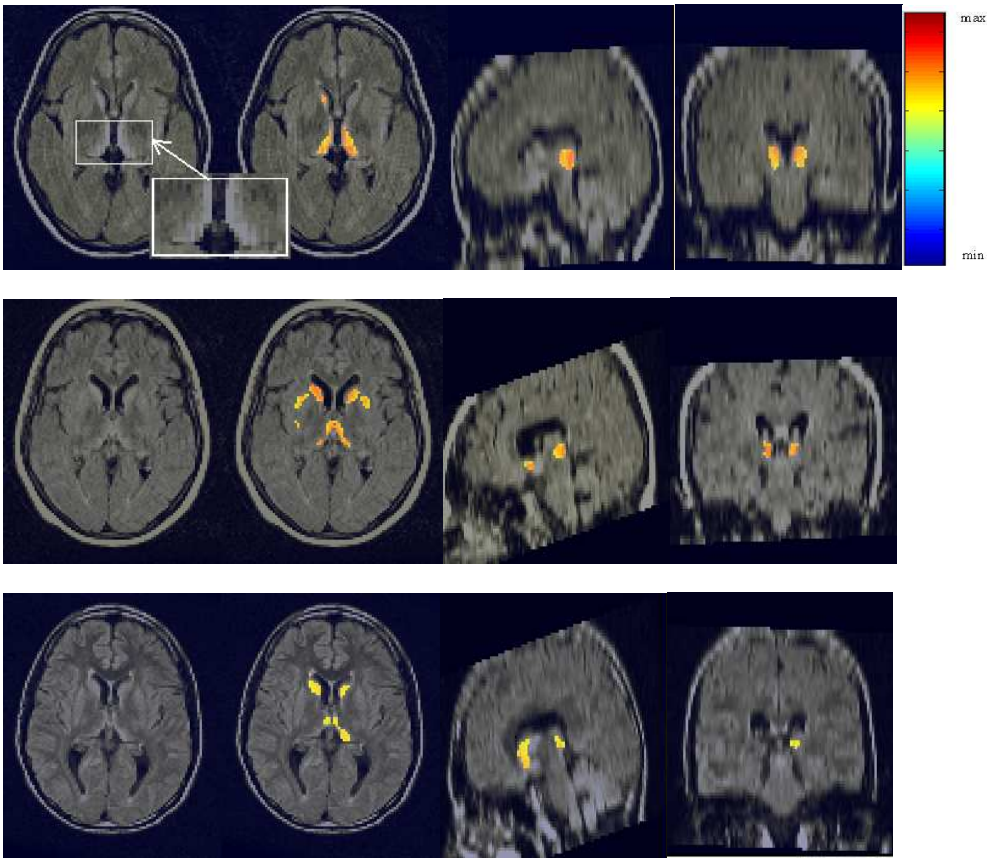

Figure 22: Results on patient data - part III. All three sets of images reported above (one row by case) originate from patients with histologically proven new-variant CJD. We present on the left a cross-section of the FLAIR MR data with abnormal hyperintensities in the internal nuclei; next to it we have the CJD detection map with corresponding intensities, as seen in the attached colourmap (note the high intensities present in the thalamic area); further to the right, we present a sagittal cross-section and a coronal cross-section with their detection maps. On the top row case on the left, we show a magnified image of the "hockey stick"-shaped thalamic hyperintensities characteristic to new-variant CJD.

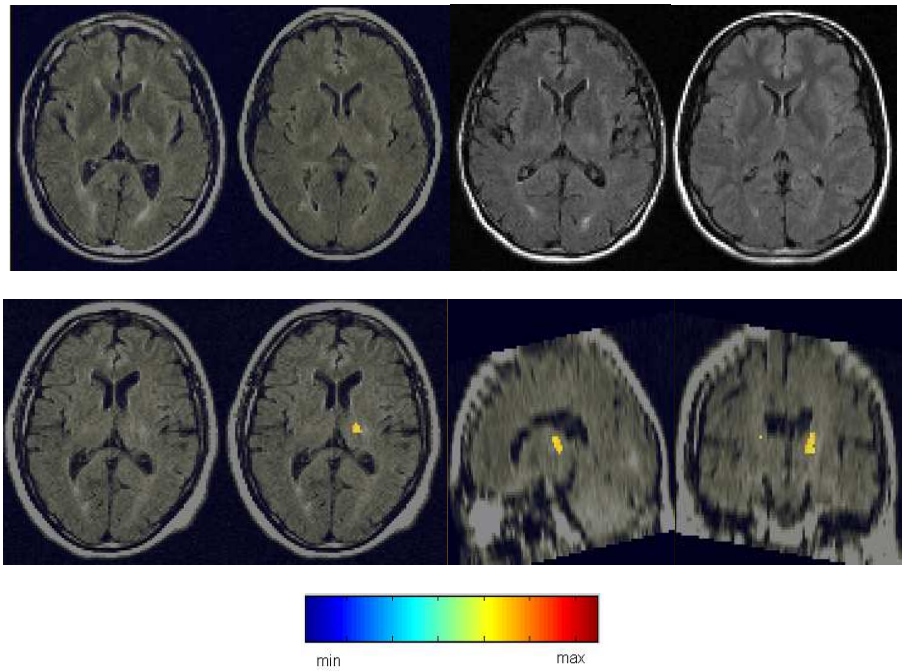

Figure 23: Results on control images from the Paris database. We show three images of controls; in the first two cases, our algorithm does not signal any false positives (FP). In the third case, a motion artefact is depicted in the left thalamus, outside of the pulvinar area.

4.2 Marseille Data

In the second part of the results section, we show examples of detection of abnormal hyperintensities in FLAIR MRI on images from patients suffering from CJD collected at the Timone Hospital in Marseille. We use T1-weighted (TE=15, TR=644), T2-weighted (TE=22, TR=4000) and FLAIR-T2 (TE=110, TR=8000, TI=2200) MR images acquired using a Siemens Magnetom Vision scanner. Our database comprises 4 sporadic CJD patient specific images, from which 2 are histologically proven, and 3 controls, which are used for the validation of the algorithm. Each patient or control has three images assigned: a T1-weighted, a T2-weighted and a T2 FLAIR sequence that are used for the registration of images and segmentation of hyperintensities. Diffusion tensor MR images are also available for all patients and controls.

We employ the same algorithm as in the previous section on Paris data; its stages are shown in Figure 19. In Figure 24, we present the detection maps on patient images with hyperintensities in basal ganglia. All sporadic CJD patients from the Marseille database show abnormal signal deviations in the internal nuclei, although at different extent. The detection results are accurate over the control images, where no hyperintensities are present nor signalled by our algorithm, as further seen in Figure 25.

The detection of abnormal intensities in basal ganglia are consistent over both databases from Paris and Marseille, although the acquisition protocols vary, as well as the MR scanners used to obtain the data. Through spatial registration and intensity normalisation, our algorithm is not sensitive to imaging conditions in the acquisition and offers good results over various data collections.

4.3 Intensity Quantitative Analysis

With the tools developed in this study, we can perform what seems to be the first computer-aided quantitative analysis between intensities in caudate nuclei or putamen, on one hand, and thalami or pulvinar nuclei, on the other hand, for CJD patients. We will refer to it as intensity quantification study (IQS). In a similar manner to the segmentation and registration of internal nuclei presented in Section 3.2, we create masks of the putamen, caudate nuclei and thalami from the Zubal Phantom registered on the MNI template (see Figure 26). Using the deformation fields of the Zubal ventricles on the patient ventricles, we align the masks of the three groups of nuclei on the patient images and segment these three anatomical regions on each patient FLAIR image. We prefer using FLAIR images before intensity normalisation for the most accurate estimation of mean values in the segmented internal nuclei.

The Zubal Phantom does not include labels for the subthalamic nuclei, such as pulvinar. According to Talairach and Tournoux [37], the pulvinar represents the "large posterior portion of the thalamus", which is "limited by a conventional verticofrontal plane through the posterior commissure" (CP). This plane (VCP) goes through the ventricular margin of CP and is perpendicular on the CA-CP biocommissural line of Talairach. We draw VCP as described above and the result is shown in Figure 27 left, where the pulvinar is marked in

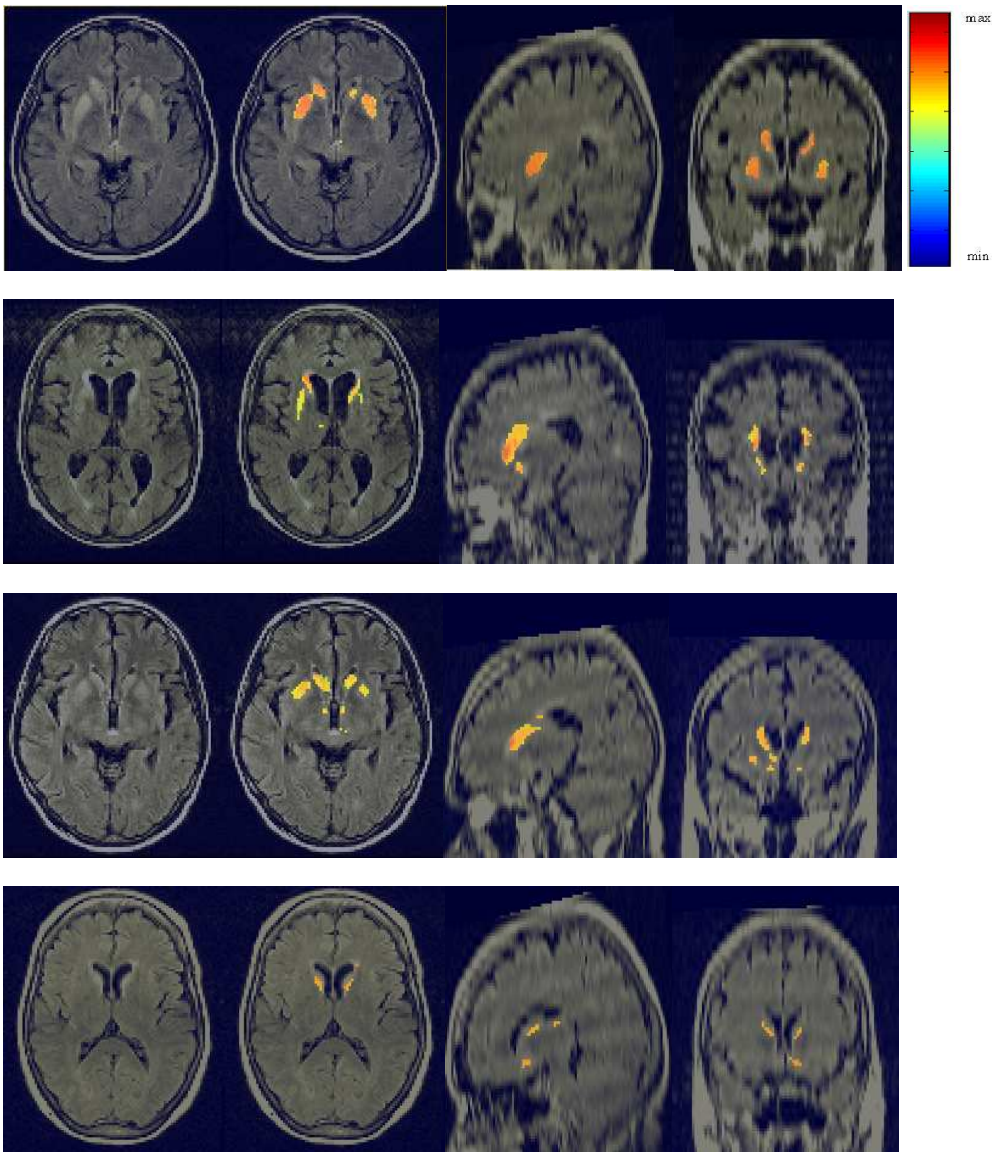

Figure 24: Results on Marseille patient data. The top two sets of images reported above (one row by case) originate from patients with histologically proven sporadic CJD. We present on the left a cross-section of the FLAIR MR data with abnormal hyperintensities in the basal ganglia; next to it we have the CJD detection map with corresponding intensities, as seen in the attached colourmap; further to the right, we present a sagittal cross-section and a coronal cross-section with their detection maps. All four image sets present abnormal intensity distributions in the deep grey nuclei, which are correctly detected by our method.

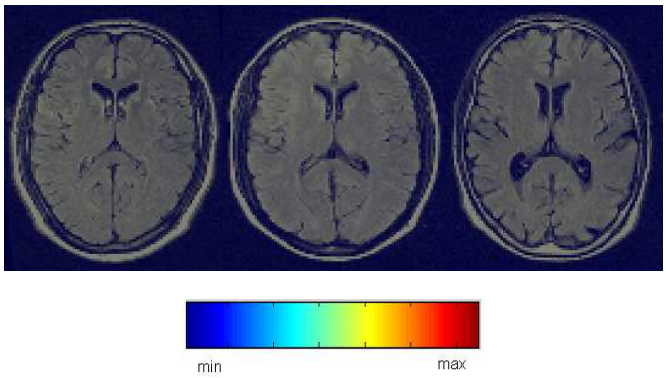

Figure 25: Results on control images from the Marseille database. We show three images of controls, where our algorithm does not signal any false positives (FP).

green. In Figure 27 right we represent in red what we call "anterior thalamus", an area in the anterior part of the thalamus (above the VCP plane), which is used to compute mean values of deep grey matter in a region with low probability to show hyperintensities in CJD patients.

We consider an intensity being significantly higher than another when their subtraction is superior in absolute value to the maximum difference between the mean intensities in either putamen or caudate nuclei and the mean intensity in thalami over all controls. See Table 1 for estimations of mean values and standard deviations in the internal nuclei in the Paris database. The results in Table 1 are consistent over the sporadic CJD patients and conform to the clinical observations.

The findings of the intensity quantification study over the data from Marseille are shown in Table 2. As expected, there is no significant difference between mean intensities in putamen or caudate nuclei versus thalami for our control data. However, there is a clear differentiation between the mean intensities in caudate nuclei and thalami in the patient data, while the putamen also show higher intensities than the thalami for two patients only.

Tables 1 and 2 show mean intensities of caudate nuclei, putamen, thalamus, pulvinar and "anterior thalamus" over the used databases. In red, we highlight the higher mean intensities, comparing values between caudate, putamen and pulvinar. All CJD cases have at least one nucleus presenting higher intensities. We note that all sporadic CJD cases have a clear hypersignal in the caudate (10/10), while the putamen is significant in 6/10 cases. Things look different in the new-variant data, where one case shows higher thalamic intensities, while the other two cases show similar behaviour to the sporadic cases. Nevertheless, all CJD cases can be differentiated from the control, although a clear separation between sporadic and new-variant cases is not obvious at this stage.

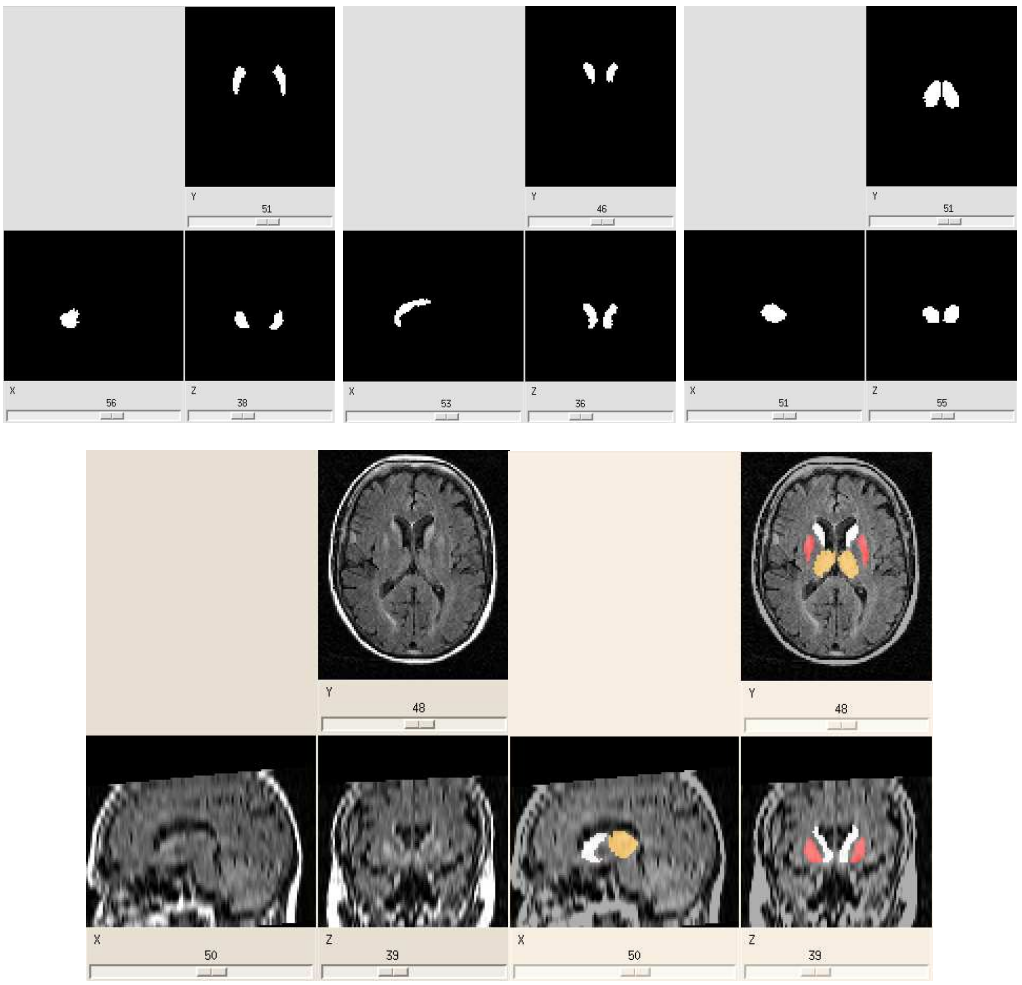

Figure 26: Segmenting the putamen, caudate nuclei and thalami in patient FLAIR images. The first mask on the left is the Zubal putamen mask; the mask in the middle is the Zubal caudate nuclei mask; the mask on the right shows the segmentation of thalami on the Zubal atlas; on the bottom row we have on the left the patient FLAIR image and on the right the results of segmentation of putamen, caudate nuclei and thalami on the patient FLAIR image (putamen in red, caudate nuclei in white and thalami in orange) after non rigid registration between the Zubal and patient ventricles.

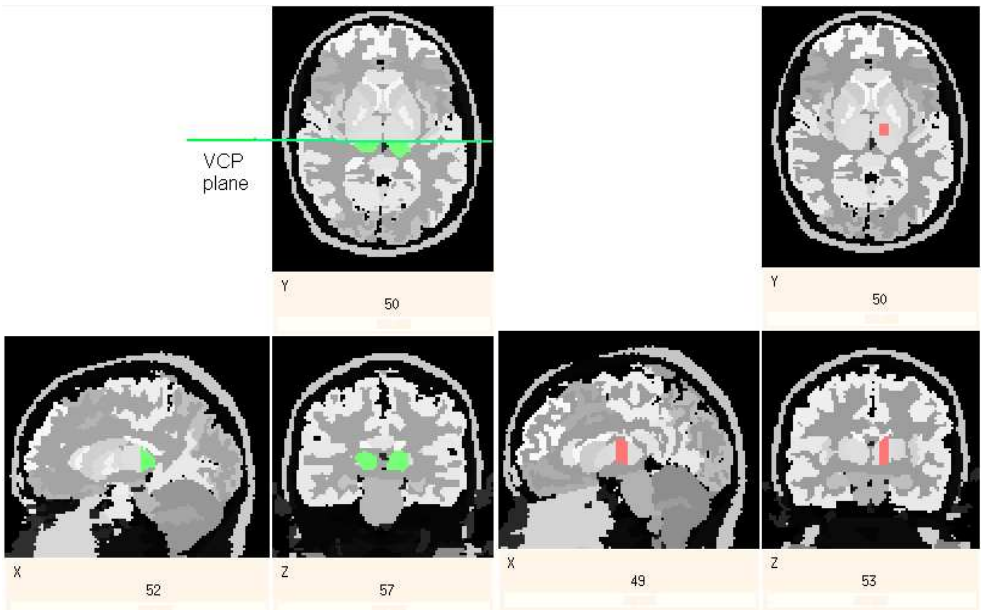

Figure 27: The definition of pulvinar and anterior thalami in the Zubal Phantom. On the left, the pulvinar is highlighted in green as the subthalamic area below the VCP plane; on the right, the "anterior thalamus" is shown in red, a depicted region in the "healthy" area of thalamus.

CJD Type	THALAMUS		PULVINAR		PUTAMEN		CAUDATE		ANTERIOR THALAMUS	
	Original FLAIR									
	Mean	STD	Mean	STD	Mean	STD	Mean	STD	Mean	STD
PS001 - sp	101.3211	17.5972	104.0977	14.5731	**124.9429**	21.1225	**124.2278**	27.4369	96.0990	16.9988
PS005 - sp	124.4844	22.8243	129.2296	17.6779	136.4809	31.0321	**140.0176**	42.3238	115.1518	18.9427
PS006 - sp	104.3543	22.0801	108.0422	18.3433	110.4657	20.7253	**117.8042**	27.3066	101.4110	23.0901
PS008 - sp	117.3514	23.8131	122.0662	20.5045	**136.6097**	34.4164	**138.5453**	45.0268	110.3905	22.5695
PS009 – sp	128.9694	25.3224	139.6038	19.0302	**161.4178**	27.3789	**165.4842**	48.2458	112.7062	21.0347
PS013 – sp	135.9345	28.1473	150.1629	20.3538	**159.7046**	25.3126	**179.0658**	52.9171	130.3907	25.1558
PS015 – nv	**168.2022**	40.2351	**184.6294**	29.9057	153.5541	17.2660	161.3147	36.8385	157.6517	28.5667
PS016 – nv	146.0991	31.2645	152.8768	29.5999	**166.8163**	22.6425	**162.7461**	37.9336	127.5112	23.9369
PS017 – nv	147.6160	33.8422	147.3342	34.9935	**164.1129**	22.3687	**166.6764**	35.9803	132.6755	17.1712
TP001 – no	99.3264	13.6407	102.1002	13.4584	94.5854	11.7682	101.6060	19.4887	94.2741	11.0484
TP002 – no	102.2425	13.7454	101.5871	11.3468	101.8790	10.9470	104.3992	19.1006	104.5873	12.8964
TP003 – no	116.8797	15.8408	120.3984	11.5168	115.5676	11.5025	119.1018	23.9813	111.9053	12.8964
TP004 – no	105.4914	14.3539	108.7742	10.5430	99.9114	12.3135	107.5106	18.9056	99.8524	9.7584
TP005 – no	126.9743	15.7937	129.1216	12.1120	127.0515	13.1008	138.6021	24.5981	120.0333	15.4481

Table 1: Mean and standard deviation values in putamen, caudate nuclei and thalami for the Paris Pitié-Salpêtrière patient data. We present results on images before intensity normalisation in order to preserve the original intensity values. The higher mean values are in red (when the difference between putamen or caudate and pulvinar mean intensities is greater than the maximum difference between these nuclei over all controls). All the sporadic data ("sp") shows higher intensities in the caudate and sometimes putamen (usually both), which verifies the reports in literature. The new-variant cases ("nv") show different behaviours at this stage with higher intensities in the pulvinar of one case and in the putamen and caudate in the other two cases. No abnormal intensities are signaled in the internal nuclei of controls ("no").

Patient	THALAMUS		PULVINAR		PUTAMEN		CAUDATE		ANTERIOR THALAMUS	
	Original FLAIR									
	Mean	STD	Mean	STD	Mean	STD	Mean	STD	Mean	STD
MT001 – sp	395.2914	60.9558	410.3537	40.3537	**467.6018**	62.8236	**488.1877**	93.2875	356.0578	90.5271
MT008 – sp	347.7698	68.2656	342.7971	67.5788	**400.1305**	62.6769	**448.5681**	108.5990	285.8062	108.1177
MT009 – sp	334.9456	50.1386	341.0581	44.1661	356.1703	50.5199	**403.1971**	82.3212	302.5980	75.3768
MT012 - sp	361.9343	45.3583	365.5803	43.5834	373.2009	45.3734	**411.4626**	70.3560	350.1048	45.2393
TM001 - no	363.7554	47.6175	371.4845	39.4533	360.5137	42.8949	383.3287	64.7482	329.6178	49.1668
TM002 - no	367.6599	46.6720	369.3134	48.6692	369.1954	38.5165	394.8521	64.7379	350.7938	58.4277
TM004 - no	376.3989	52.3517	390.9153	51.8887	365.2786	39.9349	391.1589	59.3861	349.8673	65.3041

Table 2: Mean and standard deviation values in putamen, caudate nuclei and thalami for the Marseille La Timone patient data. We present results on the original images, where MT refers to a CJD patient, while TM to a control. The superior mean values are in red (when the difference between putamen or caudate nuclei and pulvinar mean intensities is greater than the maximum difference between these nuclei over all controls). All sporadic CJD patients ("sp") have significantly higher mean intensities in the caudate nuclei and less frequent in the putamen versus thalami. Mean MR intensities in control data ("no") grey nuclei are homogeneous.

4.3.1 CJD Prompting

Intensity values in Tables 1 and 2 are different, due to the different scanners and protocols used in the neuroradiological centres where our data was acquired. In Table 3 we introduce a normalised measure for our database. We divide the mean values in the thalami, pulvinar, putamen and caudate nuclei over the mean values in the "anterior thalami" of each patient or control. We highlight in red the values in patient data that are greater than the highest value of all divisions over the control data (this value is 1.155). All patients data provides at least one suspicious value (in red) higher than 1.155. All 10 sporadic CJD cases show suspicious values in the caudate, while 8/10 in the putamen too. 2/3 new-variant cases present suspicious values in the pulvinar, while 2/3 in the putamen and caudate nuclei.

We use the input data in Table 3 and box plot the maximum value for each patient or control into two groups: 1 - CJD cases (sporadic and new-variant) and 2 - controls. We chose the maximum values in the table, as they will reflect the value in each control that is closer to the patient data and therefore less discriminant, while in patients they highlight the most suspicious grey nuclei (as not all nuclei are affected in a patient and different types of CJDs affect stronger different nuclei). The results of this box plot are shown in Figure 28. For each group of data (CJD patients or normals), the plot shows the group median value (in red line), the minimum and maximum values (at the end of the dotted lines), the upper and lower quartiles (enclosing the box around the median) and the outliers (in blue circles). Performing a T-test [8] between the two groups we get a value of $p = 1.106e^{-5}$, which gives an excellent separation between patients and controls with mean values of 1.278 for the CJD patients and 1.093 for controls (shown in red lines). The p value states that the assumption that the two classes (CJD patients and controls) are identical is significant at the 0.001 per cent level. Two outliers are depicted (shown as blue circles in Figure 28), one sporadic CJD patient (PS009) and one control (TP002), which present extreme values.

4.3.2 CJD Characterisation

We showed how CJD patients can be separated from controls using mean intensity values from pulvinar, putamen and caudate nuclei and their relation with the mean intensity within the "anterior thalamus". As expected, pulvinar intensities are more significant than mean thalamic intensities, as abnormal intensities are normally found on the pulvinar, but not throughout the thalamus. The addressed internal nuclei do not show hyperintensities for all patients (as seen in Figures 20, 21, 22 and 24), as sometimes the pulvinar or the putamen may not present abnormal distributions; the caudate appears to be the only nucleus constantly affected. Furthermore, only parts of the nucleus can show hyperintensities and therefore the mean value computed over the entire nucleus does not always reflect the degree of abnormality in the respective nucleus. It is important to compute mean intensities over the entire nucleus (i.e. pulvinar, putamen or caudate) to be able to distinguish patients from controls (which have no hyperintensities in the deep grey nuclei), as a second tool beside the hyperintensity detection shown earlier in this chapter, but we cannot yet distinguish different subgroups of patients, namely sporadic CJD from new-variant CJD. The ground

CJD Type	Thalamus/ Anterior Thalamus	Pulvinar/ Anterior Thalamus	Putamen/ Anterior Thalamus	Caudate/ Anterior Thalamus	CJD Type	Thalamus/ Anterior Thalamus	Pulvinar/ Anterior Thalamus	Putamen/ Anterior Thalamus	Caudate/ Anterior Thalamus
PS001- sp	1.0543	1.0832	**1.3001**	**1.2927**	**PS015 - nv**	1.0669	**1.1711**	0.9740	1.0232
PS005 - sp	1.0810	1.1223	**1.1852**	**1.2159**	**PS016 - nv**	1.1458	**1.1989**	**1.3082**	**1.2763**
PS006 - sp	1.0289	1.0653	1.0892	**1.1616**	**PS017 - nv**	1.1126	1.1105	**1.2369**	**1.2563**
PS008 - sp	1.0631	1.1058	**1.2375**	**1.2550**	**TM001- no**	1.0960	1.1270	1.0937	1.1427
PS009 – sp	1.1443	**1.2387**	**1.4322**	**1.4683**	**TM002 –no**	1.0294	1.0528	1.0525	1.0823
PS013 – sp	1.0425	1.1516	**1.2248**	**1.3733**	**TM004 –no**	1.0562	1.1173	1.0440	1.0927
MT001 – sp	1.0696	1.1525	**1.3133**	**1.3151**	**TP001 – no**	1.0536	1.0830	1.0033	1.0732
MT008 – sp	1.0828	**1.1994**	**1.4000**	**1.3938**	**TP002 – no**	0.9776	0.9713	0.9741	0.9981
MT009 – sp	1.0527	1.1271	**1.1770**	**1.2485**	**TP003 – no**	1.0445	1.0759	1.0327	1.0643
MT012 - sp	1.0222	1.0442	1.0660	**1.1666**	**TP004 – no**	1.0565	1.0894	1.0009	1.0785
					TP005 – no	1.0578	1.0757	1.0585	1.1547

Table 3: A normalised value to differentiate CJD patients from controls. For each CJD patient and control in the database, we divide the mean computed intensity values in the thalamus, pulvinar, putamen and caudate nucleus by the mean intensity value in the "anterior thalamus". For controls ("no"), the computed number must be closer to the ideal value of 1, which would reflect no variation in intensity over the deep grey nuclei. Since patients show abnormal intensity distributions, numbers must vary more substantially than in control. The table shows in red the values that are higher than the largest number over all nuclei and over all controls. All 10 sporadic CJD ("sp") patients show significant numbers related to the caudate nucleus and 8/10 related to the putamen. At this stage, the situation is less clear for the new-variant CJD patients ("nv"). All CJD cases how some abnormal figures, which separate them from controls.

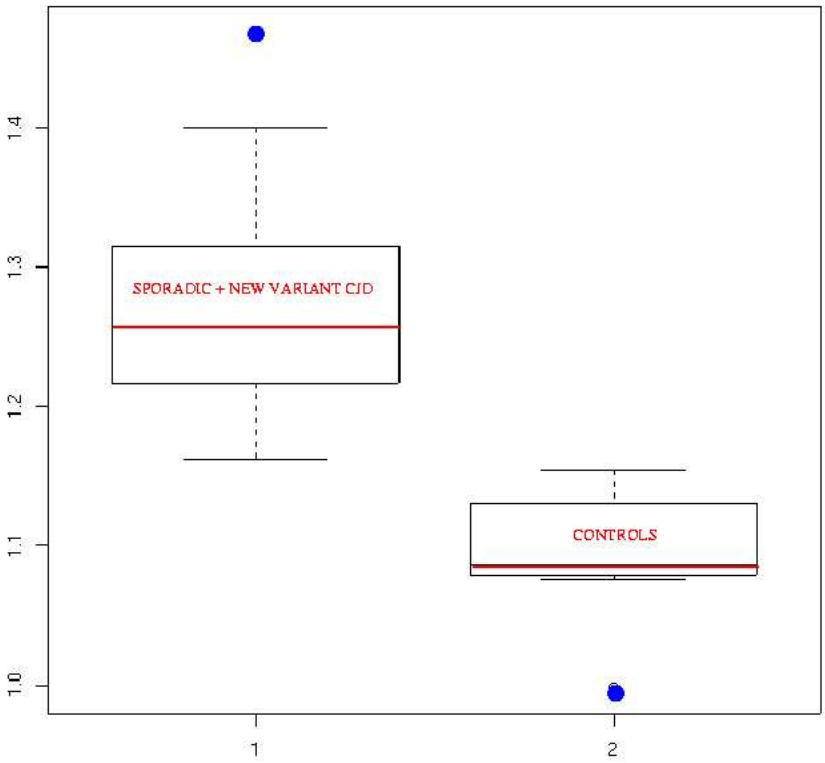

Figure 28: The box plot of the two groups: 1 - CJD patients (on the left), including the sporadic and new-variant cases; 2 -controls (on the right). The group medians are shown in red and the outliers in blue. The boxes are limited vertically by the lower and upper quartiles. Although there is some ambiguity around the maximum value in the control group and the minimum value in the patient group (where values are very close), the two groups have very distinctive distributions.

truth states that new-variant patients have higher abnormal intensities in the pulvinar than in the other deep grey nuclei, therefore we expect the relation between pulvinar and caudate to vary between the two patient groups. The abnormal intensities we will refer to are the hyperintensities found by our detection algorithm based on HVS (see Section 3.3).

We employ the masks shown in Figures 20, 21, 22 and 24 and compute mean intensity values only over the hyperintense areas. This allows us to study the relation between the abnormal intensities detected in the caudate nuclei of patients (which are relevant in each patient, as seen in Table 3) and their pulvinar (as the pulvinar is the nucleus that can discriminate sporadic cases from new-variant). We divide the mean hyperintensities in the caudate over those in pulvinar; we also present the relation between putamen and pulvinar in Table 4. When there is no hypersignal in the nucleus, this is marked as "no pulvinar" or "no putamen", whether the nucleus is the pulvinar or the putamen. In red we present values greater than 1, while number inferior to 1 are shown in blue. All 10 sporadic CJD cases have red values, while all 3 new-variant cases are presented in blue. Table 4 demonstrates the utility of the IQS to separate the two subgroups of CJD patients: sporadic and new-variant.

The box plots of the two patient subgroups is presented in Figure 29. When no pulvinar hyperintensity was detected (see PS005), we input instead the maximum value over the other sporadic cases, namely 1. 277. The two distributions are clearly different and the result of the T test shows that $p = 1.847e^{-5}$, which states that the assumption that the two classes (sporadic CJD and new-variant CJD) are identical is significant at the 0.0018 per cent level. The mean values of the two classes are 1.191 for the sporadic CJD and 0.980 for the new-variant CJD (shown in red lines).

The IQS separates on a first instance the CJD patients from healthy controls using the relation between the mean intensities in CJD most affected areas of the deep grey nuclei, (i.e. pulvinar, putamen or caudate nuclei) and the mean intensities in the "anterior thalamus", an area in the deep grey nuclei less relevant to CJD. Once the CJD cases isolated, we use the relation between the mean hyperintensities in the caudate nuclei, which stand out as the most relevant nuclei to CJD according to Table 3, and the pulvinar nuclei, the nuclei that can discriminate new-variant cases from sporadic CJD. The IQS allows to differentiate without ambiguity three distinctive classes: healthy controls, sporadic CJD patients and new-variant CJD patients.

4.4 ADC Analysis

The multisequence image acquisition protocol that we employed allowed us to explore the information contained in the apparent diffusion coefficient (ADC) maps of each patient or control data, with the exception of the new-variant cases, which were acquired using an older protocol that did not allow the computation of their ADC maps. The ADC values represent the average diffusion and can be expressed as the mean of the eigenvalues of the diffusion tensor at each voxel of the brain [21, 35]. Their computation was done using the diffusion tensor images (DTI) [42], which were included in the acquisition protocol (TE=91, TR=5300 for Paris data and TE=100, TR=6000 for Marseille data). Thus, the ADC values refer to the mobility of water in an area, which become a tissue specific measure. In an

CJD Type	Putamen/ Pulvinar	Caudate/ Pulvinar	CJD Type	Putamen/ Pulvinar	Caudate/ Pulvinar
PS001- sp	1.2310	1.2440	MT001 – sp	1.1661	1.1721
PS005 - sp	No pulvinar	No pulvinar	MT008 – sp	1.0816	1.1927
PS006 - sp	1.0609	1.0845	MT009 – sp	1.0971	1.0983
PS008 - sp	1.2301	1.1981	MT012 - sp	1.0918	1.1015
PS009 – sp	1.1448	1.2610	PS015 - nv	No putamen	0.9506
PS013 – sp	1.1168	1.2772	PS016 - nv	0.9833	0.9990
			PS017 - nv	0.9762	0.9915

Table 4: A normalised value to differentiate sporadic CJD cases from new-variant CJD. For each CJD patient in the database, we divide the mean computed hyperintensity values in the putamen and caudate nucleus by the mean hyperintensity value in the pulvinar. The main assumption is that new-variant cases ("nv") have more significant hyperintensities in the pulvinar, which allows to differentiate them from the sporadic cases ("sp"). The table shows in red the values that are greater than one, the case of all 10 sporadic CJD patients. In blue we present values smaller than 1, as in all new-variant cases. When there are no hyperintensities detected, we marked "no pulvinar" or "no putamen", according to the unaffected nucleus.

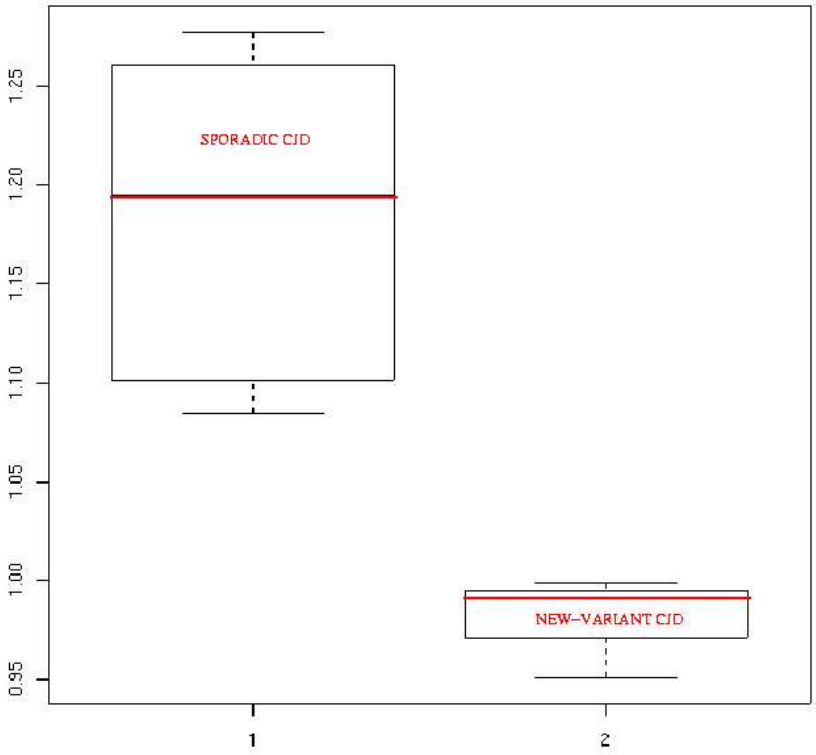

Figure 29: The box plot of the two groups: 1 - sporadic CJD patients (on the left); 2 -new-variant CJD cases (on the right). The group medians are shown in red; there are no outliers. The boxes are limited vertically by the lower and upper quartiles. The plot shows very distinctive distributions for the two groups.

application of our type, theoretically, the ADC should to be able to discriminate gliosis and spongiform changes occurring with the accumulation of prion protein [2, 18].

The ADC maps are computed directly from the raw DTI images. Once the map computed, it is registered to the MNI atlas, as in 2.2.1. We use the deep grey nuclei segmented from the Zubal Phantom and registered to the patient data, see Sections 3.2 and 4.1, to localise the putamen, thalami and caudate nuclei in the ADC maps (Figure 30). The ADC mean values and standard deviations of both Paris and Marseille data are presented in Table 5, since the ADC value is a tissue constant independent of the acquisition protocol.

Comparing controls with sporadic CJD cases over the two databases, we note lower mean ADC values in the caudate nuclei and especially the putamen of patients, probably the effect of spongiform changes. As in the intensity quantification study (IQS) in FLAIR images, the ADC values analysis confirm in a quantitative form the previous neuroradiological observation regarding the tissue changes in the brain of prion disease patients. The box plots of the two groups (1 - sporadic CJD case and 2 - controls) are shown in Figure 31. The T-test between the putamen mean intensities of the two groups gave $p = 0.0819$, which states that the assumption that the two classes (sporadic CJD and controls) are identical is significant at the 8.19 per cent level. The mean values of the two classes are 755.1 for the sporadic CJD and 804.6 for the controls (shown in red lines). In the case of caudate nuclei, $p = 0.0868$, the mean of the sporadic CJD class is 874.7 and that of controls 942.9. The outliers of distributions are shown in blue.

5 Discussions

The results presented in Tables 1,2, 3 and 4 represent a first attempt for quantitative numerical analysis of in FLAIR-T2 images MR intensities of thalamus versus putamen and caudate nucleus in CJD patients. They accurately quantify the clinical remarks related to the possible classification of different types of human spongiform encephalopathies.

All ten sporadic CJD patients have higher mean intensities in the caudate nuclei and generally putamen, as expected, although there are hyperintensities present in the pulvinar too. All patients show abnormal intensities in the deep grey nuclei, which are correctly detected by our algorithm. New-variant CJD cases show more significant hyperintensities in the pulvinar than in the other deep grey nuclei, which makes them separable from the sporadic cases. All our experimental results are in complete accordance with the neurological findings in clinical practice and with the brain lesions profile described in each form of the disease. As we do not detect any hyperintensities in controls basal ganglia (except for a movement artefact in one control found outside the pulvinar area), we neither find significant differences between the mean intensities in the three deep grey nuclei of interest (pulvinar, caudate nucleus and putamen).

Similarly, we quantify the mean ADC values in the deep grey nuclei. Once more we confirm the visually-based clinical observations, according to which we should expect lower ADC values in caudate nuclei and putamen of sporadic CJD cases, which could be due to

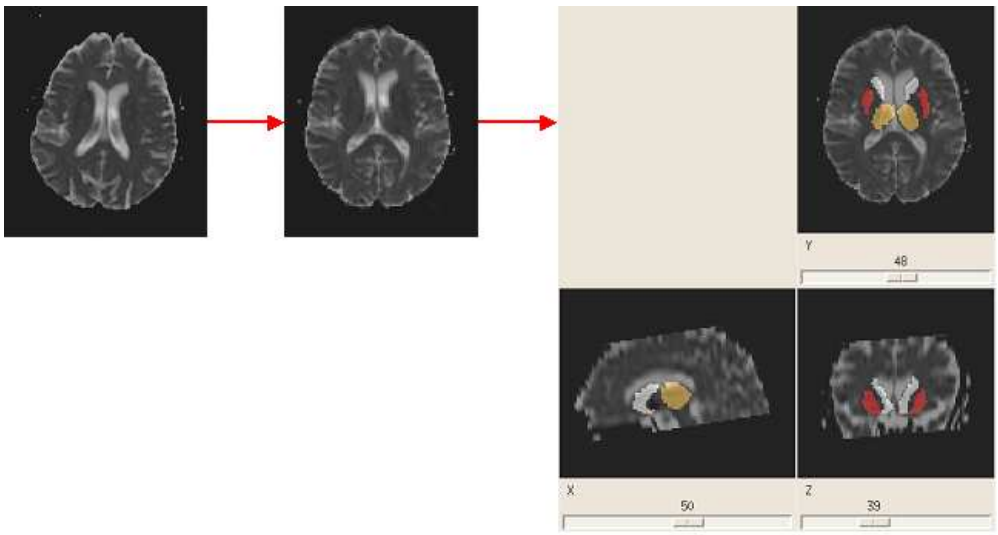

Figure 30: Segmenting the putamen, caudate nuclei and thalami in patient ADC images. From left to right: the original patient ADC image computed from the DTI images; the patient ADC images registered to the MNI atlas; the results of segmenting the putamen, caudate nuclei and thalami on the patient ADC image (putamen in red, caudate nuclei in white and thalami in orange) after the deformation of the Zubal deep grey nuclei on patient data.

CJD Type	THALAMUS		PUTAMEN		CAUDATE	
	Original ADC x 10^{-6}					
	Mean	STD	Mean	STD	Mean	STD
PS001-sp	789.3085	189.2742	691.9228	171.8785	841.7771	243.6028
PS005-sp	844.9140	175.3900	797.2171	150.4142	903.9285	259.1414
PS006-sp	780.1928	224.6700	721.3242	161.8071	779.1042	301.7885
PS008-sp	802.5221	214.6474	709.9727	176.5826	680.2277	236.3068
PS009-sp	1017.5346	138.9045	873.9627	161.0956	991.8637	202.4986
PS013-sp	915.2556	183.3820	810.1691	210.0798	924.7875	249.0524
MT001 – sp	842.132	208.468	646.871	166.586	907.210	289.693
MT008 – sp	836.653	233.727	771.659	134.771	985.356	276.355
MT009 – sp	818.547	185.842	732.405	86.045	859.918	248.481
MT012 – sp	850.054	178.328	795.938	99.890	873.030	22.3427
TP001 –no	860.5253	191.4699	776.9819	101.4538	948.4627	226.2612
TP002 –no	914.0199	186.8770	903.5494	138.4688	1071.2984	200.2259
TP003 –no	880.8245	179.1609	802.5307	94.7328	1001.1864	219.4340
TP004 – no	863.7945	172.9676	793.8540	100.9414	924.4077	211.3301
TP005 – no	862.2977	151.8246	763.9550	59.4142	922.5055	208.7846
TM001 - no	804.765	185.453	759.781	80.308	872.047	223.261
TM002 - no	841.871	164.249	815.785	70.990	895.362	214.039
TM004 - no	856.331	181.047	821.177	830.078	908.179	180.790

Table 5: ADC mean and standard deviation values in putamen, caudate nuclei and thalami for the Paris La Pitié-Salpêtrière and Marseille La Timone patient data (in mm^2/s). "Sp" refers to a sporadic CJD patient, while "no" to controls. The ADC mean values in the putamen of sporadic CJD patients are repeatedly lower than in the corresponding thalami or caudate nuclei of controls, probably caused by the spongiform changes appearing in the striatum.

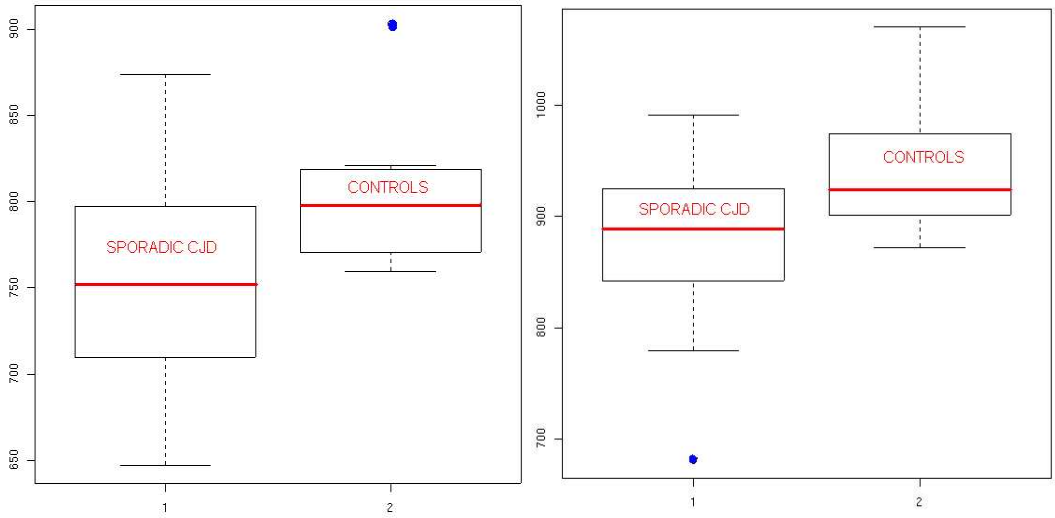

Figure 31: The box plots of the two groups: 1 - sporadic CJD patients (on the left); 2 -healthy controls (on the right). On the left we have the plots of the putamen mean intensities in the two groups; on the right the corresponding intensities in the caudate nuclei are plotted. The group medians are shown in red and the outliers in blue. The boxes are limited vertically by the lower and upper quartiles and the extremes of the groups are shown at the end of the dotted lines. The plot shows some differences between the two distribution with a p=0.08 resulting from the T-test.

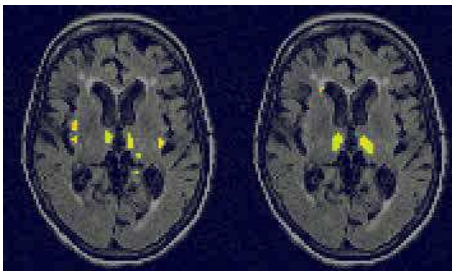

Figure 32: The improved registration at deep grey matter level removes FP while detecting correctly the abnormal signals. On the left, we see the results of detection when only a mask of ventricles was used for the non-rigid registration. On the right, the cortex outer margin is added as an anatomical boundary constraint in computing the deformation fields of the non-rigid registration, providing corrected results (see Figure 13).

spongiform changes. Results are less impressive in the ADC map and more investigations are required.

5.1 FP Analysis

In order to decrease the number of FP prompted by our detection algorithm, we refined the registration of the segmented data (the Zubal Atlas) on the patient specific data. To highlight the utility of using masks of the cortex outer boundary beside of those of ventricles (see Section 3.2), we also tested the use of masks of only ventricles (therefore without regularising the deformation within the brain). An example is shown in Figure 32 with a clear outperformance in the case using the brain boundary as an anatomical constraint, where FP are removed and the pulvinar intensities are more accurately detected. We further show in Figure 33 an example of detection without employing the smoothing procedure presented in Section 2.3. Once more, the results are superior when noise is removed preserving edges and FP are eliminated.

A good balance between the sensitivity and specificity of results is highly desirable in any computer-aided diagnosis (CAD) algorithm. In Figure 34, we show comparative results obtained by varying the minimal perceivable contrast (see Section 3.3) for better specificity or sensitivity. The effect of partial volume effects (PVE) [16] will also be investigated for removal of FP, along with the improved segmentation of ventricles by phase congruency (PC) [24]. We will also explore further quantitative analysis of MRI intensities for discriminating between the different types of human spongiform encephalopathy, when more patient data are available.

We investigated the response of well known algorithms, such as voxel-based morphometry (VBM) [1] and expectation-maximization segmentation (EMS) [39], to detect CJD-related abnormalities in brain MRI. The good contrast between brain structures is essential in

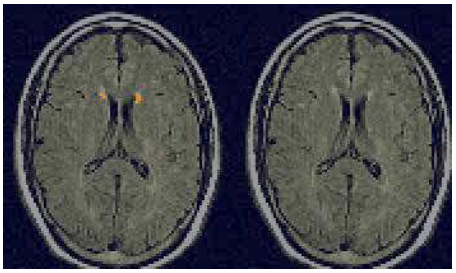

Figure 33: Removal of FP by image smoothing and edge enhancement. On the left, we see the results of detection on an image with no abnormal signal in internal nuclei; we only detect high frequency structures. On the right, the FP are removed after employing anisotropic diffusion as a preprocessing image smoother.

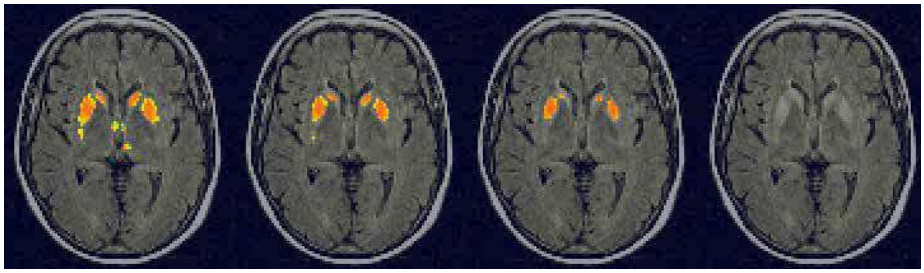

Figure 34: The influence of parameter choice in the segmentation of hyperintensity. Above, we show the same MR slice (in original on further right) with detection maps superimposed. We varied the value of the minimal perceivable contrast for higher sensitivity (further left detection map) and higher specificity (further right detection map). The results presented in Section 4 use the middle choice (second images from the left) of minimal perceivable contrast with a good balance between specificity and sensitivity.

statistically-based methods. Hence, the performance of EMS and VBM on CJD patient data, which have important artefacts and no contrast between grey matter and white matter, is inconsistent and irrelevant for clinical applications. Registration errors also influence the quality of statistical results, as comparisons between equivalent areas in normals versus patients or between different groups of patients are very sensitive to the correct delineation of the regions of interest.

5.2 Validation

We collected two series of results: one from the foveal segmentation of hyperintensities in the basal ganglia (HVS); and a second from the intensity quantification study (IQS) of intensity differences between putamen/caudate/pulvinar nuclei versus "anterior thalamus". Thus, our database comprises 13 patients, from which 10 sporadic CJD cases and 3 new-variant CJD cases, and 8 controls. All patient MRI sets show hyperintensities in the zone of interest. The validation results are presented in Table 6. With a combination of HVS and IQS, we are able to prompt 13/13 prion disease cases with no FP amongst the controls. We detect all cases of hyperintensities in the basal ganglia employing the foveal segmentation of signal deviations.

In Table 6, both HVS and IQS algorithms prompt correctly the suspicious cases of CJD and the logical 'and' (when both HVS and IQS must prompt a case simultaneously) shown in the last row of the table may seem redundant. To prove its utility, we bring to the attention of the reader the case of a patient with a severe brain atrophy (see Figure 35). The patient was initially included in the CJD database, but the histological tests proved that there was not a prion disease. The radiological exam found areas of possible stronger intensity in the pulvinar, which combined with the signs of dementia led to an obvious case for a FP for CJD diagnosis. Our HVS detection algorithm also detected abnormal areas in the thalamus, but of low intensity. The results of IQS was nevertheless neutral, with similar mean intensities in the pulvinar (129.3), putamen (127.5) and caudate nuclei (128.2). When we divided these values to the mean intensity over the "anterior thalamus" (199.3), we obtain a maximum value of 1.084, which is inferior to the threshold that separates CJD cases from normals (1.155). Therefore, although the HVS detection of hyperintensities prompted suspicious intensity distributions in the pulvinar (in accordance with the neuroradiological observations), a logical 'and' between HVS and IQS (as in Table 6) discarded this case from the possible CJD cases. Nevertheless, the case is valuable for testing the non-rigid deformation in this extreme case between the Zubal Phantom ventricles and the large ventricles of this patient, as seen in Figure 24 on the second row. While there are small abnormalities in the patient's MRI, its data could not be included in the control database.

The detection of deep grey nuclei hyperintensities confirms the previous visually-based clinical observations according to which the FLAIR/T2 MR images of sporadic CJD patients show hypersignals in the caudate nuclei. Quantifying the intensities in thalami, caudate nuclei and putamen, we prove that there are always higher mean intensities in the caudate nuclei (10/10) and sometimes putamen (6/10) than the pulvinar for the same sporadic CJD patients. The caudate nucleus is also of high intensity in the new-variant CJD cases. This

	CJD Cases		Controls	False Positives
	Sporadic	New Variant		(FP)
Human Visual System (HVS)	**10/10**	**3/3**	**0/8**	**0/21**
Intensity Quantification Study (IQS)	**10/10**	**3/3**	**0/8**	**0/21**
HVS and IQS	**10/10**	**3/3**	**0/8**	**0/21**

Table 6: The validation of our algorithm. We present detection results using: (i) the foveal segmentation of hyperintensities in basal ganglia (HVS); (ii) the intensity quantification study (IQS); (iii) a logical 'and' between HVS and IQS. While a both HVS and IQS give excellent results when employed separately, a combination of the two is desired for the best detection results to reject FP as seen in Figure 35.

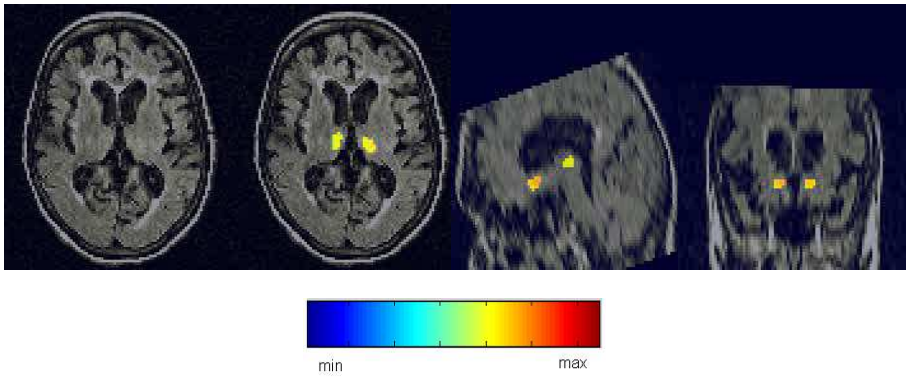

Figure 35: Results on image data from a patient presenting a significant brain atrophy. The patient was suspect of CJD after the radiological examination, but the histological results proved that there is no prion infection present. There are still high intensities (of a lower scale) in the thalami, as our detection algorithm reflects correctly.

conclusion highlights the caudate nuclei as area of interest for the diagnosis of CJD, in complete agreement with the neuropathological findings. The relevance of caudate nuclei is also underlined by the decreased quantified mean ADC values in patient versus normal data. With zero FP, our method of detection and quantification of basal ganglia intensity distributions proves to reach maximum specificity with very high sensitivity. We differentiate without ambiguity all CJD cases (sporadic and new-variant) from healthy controls. Moreover, the study of hyperintensities in the deep grey nuclei delineates different characteristics between new-variant and sporadic CJD cases, in accordance with the clinical observations, which allows us to characterise the CJD patients into two subgroups of human spongiform encephalopathies, sporadic and new-variant.

6 Conclusion

We presented a method for the detection of hypersignals in grey matter internal nuclei from multisequence MR images. The particular context of our application aims to indicate the presence of human spongiform encephalopathies, prion protein diseases here referred as Creutzfeldt-Jakob Diseases (CJD). The technique employs intensity and spatial normalisation, noise removal with feature enhancement, foveal segmentation for the detection of hyperintensities and a priori anatomical information for refined registration and removal of false positives.

Our method further allows the quantification of intensity distributions in basal ganglia, a discrimination criterion between patients and normals, which confirms the visually-based radiological observations related to CJD. The caudate nuclei are highlighted as main areas of diagnosis of sporadic CJD, in agreement with the histological data. The caudate nuclei and putamen show more significant hypersignal than in pulvinar in sporadic CJD patient FLAIR data. In new-variant CJD patients, we find more significant hyperintensities in the pulvinar than in the other internal nuclei. The relevance of caudate nuclei and putamen is also underlined by their decreased quantified ADC values in patient versus normal data, probably due to the accumulation of pathological prion protein. The intensity quantification study is further developed for better detection results with a view to discriminate between the different types of prion diseases. The detection results are in accordance with the clinical ground truth. Our study demonstrates the value of MRI for a prospective non-invasive diagnosis of sporadic CJD and the characterisation of prion diseases, as we clearly differentiate sporadic from new-variant CJD cases. More validation will be performed in future work, when a larger database is available.

In this preliminary study, our method proves as reliable as the interpretation of radiologists for the detection of basal ganglia hypersignals. Moreover, it allows to automatically obtain quantitative data from MR patients with CJD, which could be used for the follow-up, whether a treatment is available or not.

Acknowledgements

This work is funded by the GIS-Prions project (see the partaking centres under the authors names) coordinated by Jean-Philippe Brandel.

References

[1] J. Ashburner and K.J. Friston. Voxel-based morphometry - the methods. *NeuroImage*, 11:805–821, 2000.

[2] M.M. Bahn, D.K. Kido, W. Lin, and A.L. Pearlman. Brain magnetic resonance diffusion abnormalities in imaging in creutzfeldt-jakob disease. *Arch Neurol*, 54:1411–1415, 1997.

[3] M.M. Bahn and P. Parchi. Abnormal diffusion-weighted magnetic resonance images in Creutzfeldt-Jakob disease. *Arch Neurol*, 56:577–583, 1999.

[4] J.P. Brandel. Clinical aspects of human spongiform encephalopathies, with the exception of iatrogenic forms. *Biomed Pharmacother*, 53:14–18, 1999.

[5] J.P. Brandel, N. Delasnerie-Laupretre, J.L. Laplanche, J.J. Hauw, and A. Alpetrovitch. Diagnosis of Creutzfeldt-Jakob disease: Effect of clinical criteria on incidence estimates. *Neurology*, 54:1095–1099, 2000.

[6] M A. Brown and R.C. Semelka. MR imaging abbreviations, definitions, and descriptions: A review. *Radiology*, 213:647–662, 1999.

[7] P. Cachier, E. Bardinet, D. Dormont, X. Pennec, and N. Ayache. Iconic feature-based nonrigid registration: The PASHA algorithm. *CVIU — Special Issue on Nonrigid Registration*, 89(2-3):272–298, Feb.-March 2003.

[8] C. Chatfield. *Statistics for Technology: A Course in Applied Statistics*. Chapman and Hall, 3rd edition, 1983.

[9] D.L. Collins, A.P. Zijdenbos, V. Kollokian, J.G. Sled, N.J. Kabani, C.J. Holmes, and A.C. Evans. Design and construction of a realistic digital brain phantom. *IEEE Transactions on Medical Imaging*, 17(3):463–468, 1998.

[10] A. Coulthard, K. Hall, P.T. English, P.G. Ince, D.J. Burn, and D. Bates. Quantitative analysis of mri signal intensity in new variant Creutzfeldt-Jakob disease. *The British Journal of Radiology*, 72:742–748, 1999.

[11] J.A. de Priester, G.H. Jansen, J.R. de Kruijk, and J.T. Wilmink. New MRI findings in Creutzfeldt-Jakob disease: High signal in the globus pallidus on T1-weighted images. *Neuroradiology*, 41:265–268, 1999.

[12] P. Demaerel, A. Baert, W. Vanopdensboch, and R. Robberecht. Diffusion weighted magnetic resonance imaging in Creutzfeldt-Jakob disease: Research letter. *The Lancet*, 349:847–848, 1997.

[13] D. Dormont. New variant of Creutzfeldt-Jakob disease. *Euro Surveil*, 5(9):95–97, 2000.

[14] M. Finkenstaedt, A Szudra, I. Zerr, S. Poser, J. Hise, J. Stoebner, and T. Wener. MR imaging of Creutzfeldt-Jakob disease. *Radiology*, 3:793–798, 1991.

[15] H.J Gertz, H. Henkes, and J. Cervos-Navarro. Creutzfeldt-jakob disease: Correlation of MRI and neuropathologic findings. *Neurology*, 38(9):1481–1482, 1988.

[16] M. A. González Ballester, A. Zisserman, and M. Brady. Estimation of the partial volume effect in MRI. *Medical Image Analysis*, 6(4):389–405, 2002.

[17] S. Haik, J.P. Brandel, C. Oppenheim, V. Sazdovitch, J.J. Dormont, D. Hauw, and C. Marsault. Sporadic CJD mimicking variant CJD with bilateral increased signal in the pulvinar. *Neurology*, 58:148–149, 2002.

[18] S. Haik, D. Dormont, B.A. Faucheux, C. Marsault, and J.J. Hauw. Prion protein deposits in magnetic resonance imaging signal abnormalities in Creutzfeldt-Jakob disease. *Annals of Neurology*, 51(6):797–799, June 2002.

[19] A. Hojjat, D. Collie, and A.C.F. Colchester. The putamen intensity gardient in CJD diagnosis. In T. Dohi and R. Kikinis, editors, *Medical Imaging And Computer Assisted Surgery (MICCAI 2003)*, volume 2488 of *Lectures Notes in Computer Science*, pages 524–531. Springer, 2003.

[20] J P. Hornak. The basics of MRI. http://www.cis.rit.edu/htbooks/mri/.

[21] E.W. Hsu and S. Mori. Analytical expressions for the nmr apparent diffusion coefficients in an anisotropic system and a simplified method for determining fiber orientation. *Magnetical Resonance in Medicine*, 34:194–200, 1995.

[22] D.E. Job, S. Whalley, H.C. ad McConnell, M. Glabus, E.C. Johnstone, and S.M. Lawrie. Structural gray matter differences between first-episode schizophrenics and normal controls using voxel-based morphometry. *Neuroimage*, 17:880–889, 2002.

[23] G.B. Karas, E.J. Burton, S.A.R.B. Rombouts, R.A. van Schijndel, J.T. O'Brien, P. Scheltens, I.G. McKeith, D. Williams, C. Ballard, and F. Brakhof. A comprehensive study of gray matter loss in patients with Alzheimer's disease using optimized voxel-based morphometry. *Neuroimage*, 18:895–907, 2003.

[24] M. G. Linguraru, M. A. González Ballester, and N. Ayache. A multiscale feature detector for morphological analysis of the brain. In Randy E.E. and Terry M.P., editors, *Proc. of MICCAI'03*, volume 2879 of *LNCS*, pages 738–745, Montreal, Canada, nov 2003. Springer Verlag.

[25] M.G. Linguraru. *Feature Detection in Mammmographic Image Analysis.* PhD thesis, University of Oxford, 2002.

[26] J.C. Mazziotta, A.W. Toga, A.C. Evans, P.T. Fox, J. Lancaster, K. Zilles, R.P. Woods, T. Paus, G. Simpson, B. Pike, C.J. Holmes, D.L. Collins, P.M. Thompson, D. MacDonald, M. Iacoboni, T. Schormann, K. Amunts, N. Palomero-Gallagher, S. Geyer, L. Parsors, K.L. Narr, N. Kabani, G. Le Goualher, M. Boomsma, T. Cannon, R. Kawashima, and B. Mazoyer. A probabilistic atlas and reference system for the human brain: International consortium for brain mapping (ICBM). *Philosophical Transactions of the Royal Society of London, Series B (Biological Sciences)*, 356(1412):1293–1322, 2001. Enclosed in Appendix II.

[27] W. Milton, S. Atlas, E. Lavi, and J. Moliman. Magnetic resonance imaging of Creutzfeldt-Jakob disease. *Annals of Neurology*, 29:438–440, 1991.

[28] M. Onofrj, T. Fulgente, D. Gambi, and G. Macchi. Early MRI findings in Creutzfeldt-Jakob disease. *Journal of Neurology*, 240:423–426, 1993.

[29] C. Oppenheim, J.P. Brandel, J.J. Hauw, J.P. Deslys, and B. Fontaine. MRI and the second French case of vCJD. *Lancet*, 356:253–254, 2000.

[30] S. Ourselin. *Recalage d'Images Médicales par Appariement de régions - Application à la Construction d'Atlas Histologiques 3D.* PhD thesis, Université de Nice - Sophia Antipolis, 2002.

[31] S. Ourselin, A. Roche, S. Prima, and N. Ayache. Block matching: A general framework to improve robustness of rigid registration of medical images. In A.M. DiGioia and S. Delp, editors, *Third International Conference on Medical Robotics, Imaging And Computer Assisted Surgery (MICCAI 2000)*, volume 1935 of *Lectures Notes in Computer Science*, pages 557–566, Pittsburgh, Pennsylvanie USA, octobre 11-14 2000. Springer.

[32] G.S. Pearl and R.E. Anderson. Creutzfeldt-jakob disease: High caudate signal on magnetic resonance imaging. *South Med J*, 82:1177–1180, 1989.

[33] D. Rey, G. Subsol, H. Delingette, and N. Ayache. Automatic detection and segmentation of evolving processes in 3D medical images: Application to multiple sclerosis. *Medical Image Analysis*, 6:163–179, 2002.

[34] A. Schroeter, I. Zerr, K. Henkel, and H.J. Tschampa. Magnetic resonance imaging in the clinical diagnosis ofCreutzfeldt-Jakob disease. *Arch Neurol*, 57:1751–1757, 2000.

[35] S. Skare. *Optimisation Strategies in Diffusion Tensor MR Imaging.* PhD thesis, Karolinska University Press, 2002.

[36] D.D. Stark, W.G. Bradley, and W.G. Jr. Bradley. *Magnetic Resonance Imaging.* Mosby, 3rd edition, 1999.

[37] J. Talairach and P. Tournoux. *Co-Planar Stereotaxic Atlas of the Human Brain.* Thieme Medical Publishers, 1988.

[38] H. Urbach, J. Klisch, HK. Wolf, and et al. MRI in sporadic Creutzfeldt-Jakob disease: correlation with clinical and neuropathological data. *Neuroradiology*, 40:65–70, 1998.

[39] K. Van Leemput. *Quantitative Analysis of Signal Abnormalities in MR Imaging for Multiple Sclerosis and Creutzfeldt-Jakob Disease.* PhD thesis, Katholieke Universiteit Leuven, 2001.

[40] K. Van Leemput, F. Maes, D. Vandermeulen, A. Colchester, and P. Suetens. Automated segmentation of multiple sclerosis lesions by model outlier detection. *IEEE Transactions on Medical Imaging*, 20(8):677–688, 2001.

[41] J. Weickert. *Anisotropic Diffusion in Image Processing.* B.G. Teubner, 1st edition, 1998.

[42] C.F. Westin, S.E. Maier, B. Khidhir, P. Everett, F.A. Jolesz, and R. Kikinis. Image processing for Diffusion Tensor Magnetic Resonance Imaging. In *Medical Imaging And Computer Assisted Surgery (MICCAI 1999)*, Lectures Notes in Computer Science, pages 441–452. Springer, 1999.

[43] R.G. Will, M. Zeidler, G.E. Stewart, M.A. Macleod, J.W. Ironside, S.N. Cousens, J. Mackenzie, K. Estibeiro, A.J.E. Green, and R.S.G. Knight. Diagnosis of new variant Creutzfeldt-Jakob disease. *Ann Neurol*, 47:575–582, 2000.

[44] M. Zeidler, R.J. Sellar, D.A. Collie, R.S.G. Knight, G.E. Stewart, M.A. Macleod, J.W. Ironside, S.N. Cousens, A.F.C. Colcester, D.M. Hadley, and R.G. Will. The pulvinar sign on magnetic resonance imaging in variant Creutzfeldt-Jakob disease. *The Lancet*, 355:1412–1418, April 2000.

[45] I.G. Zubal, C.R. Harrell, E.O. Smith, Z. Rattner, G. Gindi, and P.B. Hoffer. Computerized three-dimensional segmented human anatomy. *Medical Physics*, 21:299–302, 1994.

Unité de recherche INRIA Sophia Antipolis
2004, route des Lucioles - BP 93 - 06902 Sophia Antipolis Cedex (France)

Unité de recherche INRIA Futurs : Parc Club Orsay Université - ZAC des Vignes
4, rue Jacques Monod - 91893 ORSAY Cedex (France)
Unité de recherche INRIA Lorraine : LORIA, Technopôle de Nancy-Brabois - Campus scientifique
615, rue du Jardin Botanique - BP 101 - 54602 Villers-lès-Nancy Cedex (France)
Unité de recherche INRIA Rennes : IRISA, Campus universitaire de Beaulieu - 35042 Rennes Cedex (France)
Unité de recherche INRIA Rhône-Alpes : 655, avenue de l'Europe - 38334 Montbonnot Saint-Ismier (France)
Unité de recherche INRIA Rocquencourt : Domaine de Voluceau - Rocquencourt - BP 105 - 78153 Le Chesnay Cedex (France)

Éditeur
INRIA - Domaine de Voluceau - Rocquencourt, BP 105 - 78153 Le Chesnay Cedex (France)
http://www.inria.fr
ISSN 0249-6399